nature geoscience

SUPPLEMENTARY INFORMATION

https://doi.org/10.1038/s41561-018-0233-2

In the format provided by the authors and unedited.

Observational evidence for active dust storms on Titan at equinox

S. Rodriguez [1*], S. Le Mouélic [2], J. W. Barnes [3], J. F. Kok [4], S. C. R. Rafkin [5], R. D. Lorenz [6], B. Charnay [7], J. Radebaugh [8], C. Narteau [1], T. Cornet [9], O. Bourgeois [2], A. Lucas [1], P. Rannou [10], C. A. Griffith [11], A. Coustenis [7], T. Appéré [12], M. Hirtzig [7,20], C. Sotin [13], J. M. Soderblom [14], R. H. Brown [11], J. Bow [3], G. Vixie [3], L. Maltagliati [1,21], S. Courrech du Pont [15], R. Jaumann [16], K. Stephan [16], K. H. Baines [17], B. J. Buratti [13], R. N. Clark [18] and P. D. Nicholson [19]

[1]Institut de Physique du Globe de Paris, Sorbonne Paris Cité, Univ Paris Diderot, UMR 7154 CNRS, Paris, France. [2]Laboratoire de Planétologie et Géodynamique (LPGNantes), CNRS-UMR 6112, Université de Nantes, Nantes, France. [3]University of Idaho, Department of Physics, Moscow, ID, USA. [4]Department of Atmospheric and Oceanic Sciences, University of California, Los Angeles, CA, USA. [5]Planetary Atmospheres and Surfaces, Department of Space Studies, Southwest Research Institute, Boulder, CO, USA. [6]Johns Hopkins University Applied Physics Laboratory, Laurel, MD, USA. [7]LESIA, Observatoire de Paris, PSL-Research Univ., CNRS, Univ. Pierre et Marie Curie Paris 06, Sorbonne Univ., Univ. Paris-Diderot, Sorbonne Paris-Cité, Meudon, France. [8]Department of Geological Sciences, Brigham Young University, Provo, UT, USA. [9]European Space Agency (ESA), European Space Astronomy Centre (ESAC), Villanueva de la Canada, Spain. [10]Groupe de Spectroscopie Moléculaire et Atmosphérique, UMR CNRS 6089, Université de Reims, U.F.R. Sciences Exactes et Naturelles, Reims, France. [11]Department of Planetary Sciences, University of Arizona, Lunar and Planetary Laboratory, Tucson, AZ, USA. [12]Institut de Planétologie et d'Astrophysique de Grenoble, Université J. Fourier, CNRS/INSU, Grenoble, France. [13]California Institute of Technology/Jet Propulsion Laboratory, Pasadena, CA, USA. [14]Department of Earth, Atmospheric and Planetary Sciences, Massachusetts Institute of Technology, Cambridge, MA, USA. [15]Laboratoire Matière et Systèmes Complexes, Université Paris Diderot, Paris, France. [16]German Aerospace Centre (DLR), Institute of Planetary Research, Berlin, Germany. [17]Space Science and Engineering Center, University of Wisconsin, Madison, WI, USA. [18]Planetary Science Institute, Tucson, AZ, USA. [19]Department of Astronomy, Cornell University, Ithaca, NY, USA. [20]Present address: Fondation 'La main à la pâte', Montrouge, France. [21]Present address: Springer Nature, London, UK. *e-mail: rodriguez@ipgp.fr

Supplementary Information for

Dust storms on Titan

This PDF file includes:

Figs. S1 to S8

Tables S1 to S6

References (*41*) to *(50)*

Table of contents

1. Timing and location of the T56, T65 and T70 brightening events

A

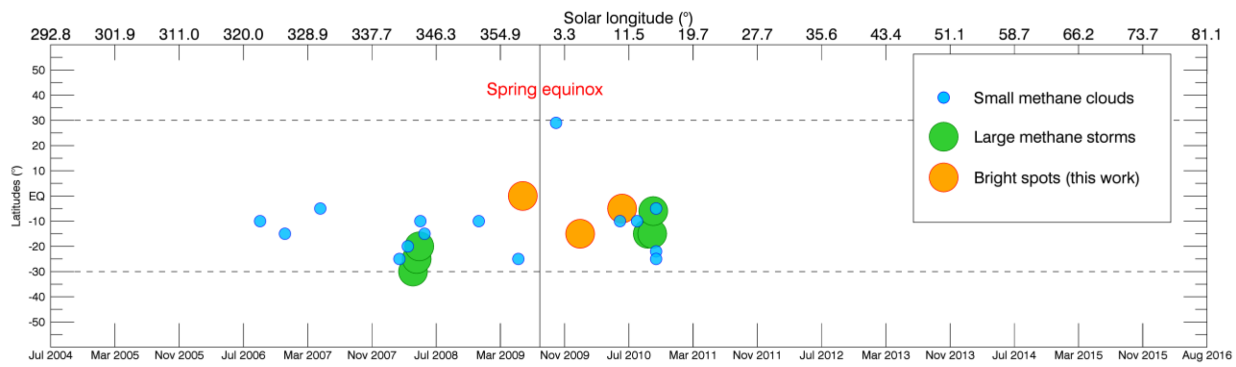

B

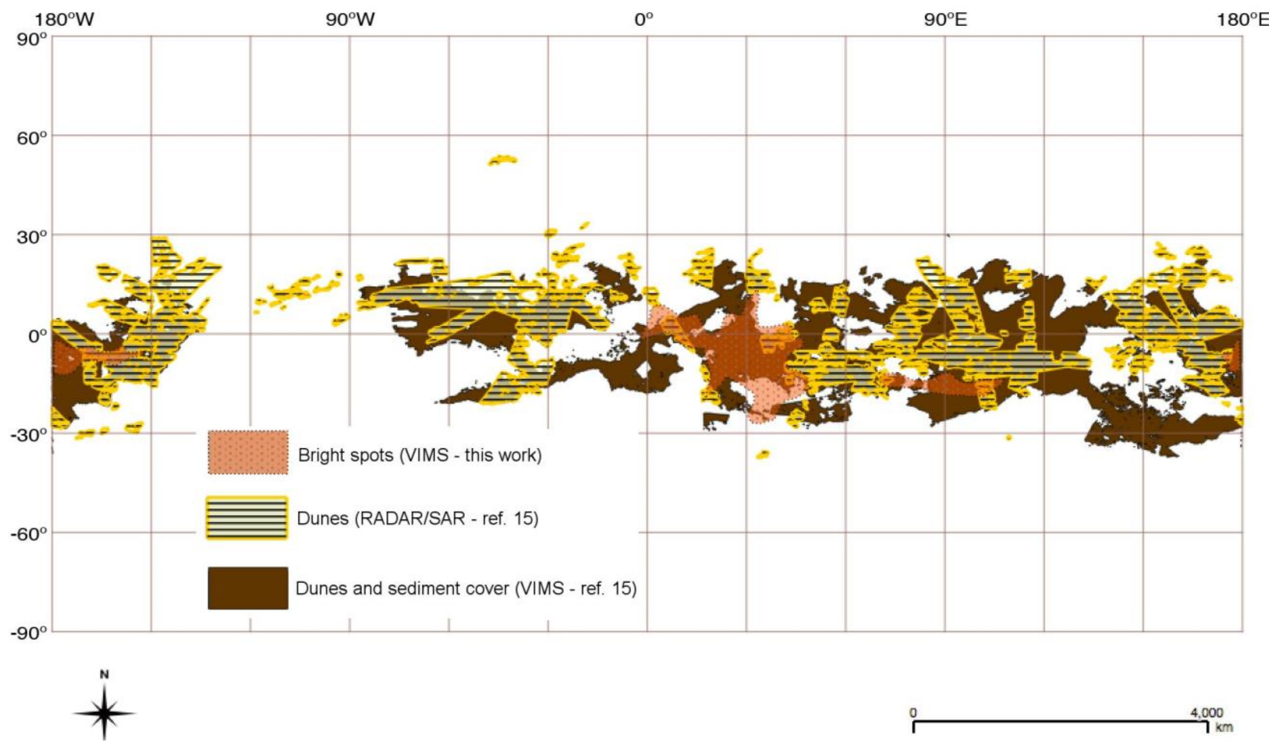

Fig. S1. (a) Timing of the T56, T65 and T70 brightening events. We report here all the clouds observed in the tropical belt of Titan by Cassini ISS and VIMS instruments[3-5,13] and from ground-based telescopes[12], since the beginning of the Cassini mission (1st of July, 2004) to the present day. Titan solar longitudes are indicated on the top x-axis (northern spring equinox is Ls = 0°). They all occurred very close in time to the northern spring equinox (vertical black line). No meteorological activity was detected between +30° and -30° latitudes before mid-2006 and after October 2010. In between those dates, only 15 small tropical clouds were detected (blue dots). Nevertheless, their frequency and size constantly grew approaching equinox. Just before and after equinox, Cassini and Earth-based observations spotted two large storms (green dots) around April 2008 and October 2010, probably associated with intense rainfall[5,12]. Even closer to the equinox, when the Sun was directly illuminating the equator, three singular and intense equatorial brightenings, suspected to be related to energetic dust storms, were detected (orange dots) (this work). All these observations constitute indubitable clues that the equatorial belt of Titan experiences a prominent meteorological activity, which affects the surface in those regions, during a short period of time around the equinoxes. **(b) Location of the T56, T65 and T70 brightening events.** We present the global map of Titan's dune fields seen by the Cassini/RADAR (hatched yellow areas) and dune sediment cover derived from Cassini/VIMS (brownish areas), adapted from ref. (*15*). The areas covered by the T56, T65 and T70 brightenings are outlined in orange. Note the striking geographic correspondence between the T56, T65 and T70 brightening areas and regions dominated by dunes and/or organic sediment.

2. Spectral characteristics of the T56, T65 and T70 brightenings as seen with VIMS spectro-images

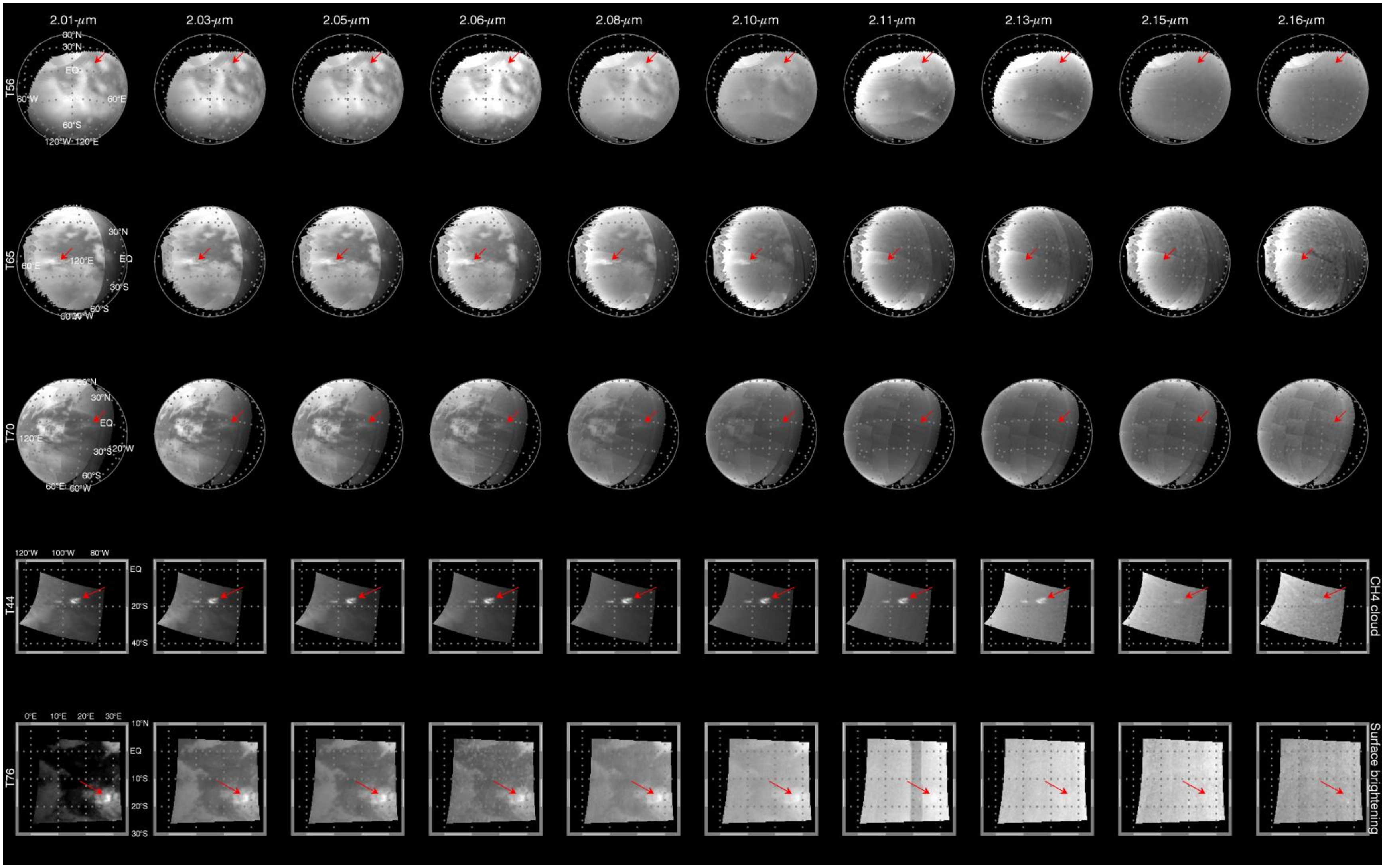

Fig. S2. Spectral altitude estimator for the T56, T65, T70 bright spots. We compare Titan VIMS images of the T56, T65, T70 bright spots with those of a confirmed methane cloud seen in the tropics at T44 (28 May 2008)[3,4,13] and a surface brightening event observed at T76 (8 May 2011)[6] [rows] from the center (2.01-µm) to the far-wing (2.16-µm) of the 2-µm methane window [columns]. Red arrows point to the bright spots studied here, the T44 cloud and the surface bright spot. The height of the top of any reflective layer (a cloud of suspended particles) in Titan's atmosphere can be approximated by the wavelengths at which it can be seen. Between 2.01 and 2.16-µm, the methane opacity increases (as for any other methane windows). If a cloud can be seen at wavelengths of strong methane opacity, then it must be high in the atmosphere where less methane is above it. If a cloud does not appear until wavelengths of low methane opacity, it is much lower in the atmosphere. With the hyperspectral images from VIMS, the wavelength at which a cloud first appears can be assessed. At 2.01-µm, the surface, methane cloud, and T56, T65 and T70 brightenings are all visible. By 2.11-µm the surface (and the surface brightening) is no longer visible, the clouds can still be seen, but the bright spots start dimming. At 2.13-µm the bright spots are no longer visible; only the methane clouds can be seen, remaining visible until 2.16-µm. It is worth noting that the three spots are observed with a more favorable geometry (with lower airmass) than the cloud and the surface brightening, indicating that their disappearing at a shorter wavelength is not due to geometric effects. This spectral behavior demonstrates that the bright spots seen at T56, T65 and T70 are below the methane cloud (the T44 cloud top has been measured at 16±4 km altitude (ref. *13*) and above the surface. Comprehensive radiative transfer calculations will allow us to determine their altitude more accurately.

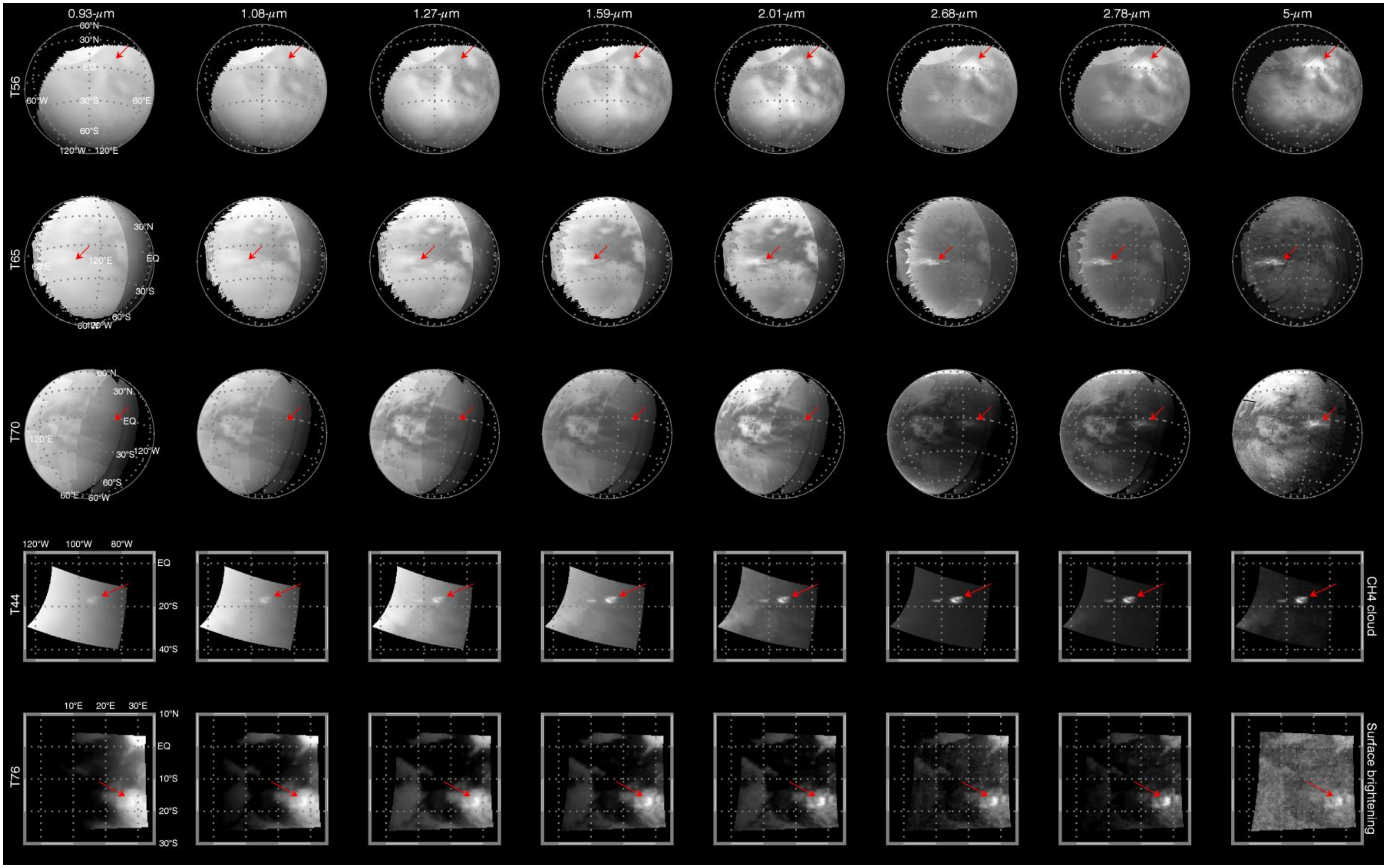

Fig. S3. Overall spectral behavior of T56, T65, T70 bright spots over the VIMS wavelength range. We compare here Titan VIMS images of the T56, T65, T70 bright spots (this work), T44 methane cloud[3-5,13] and T76 surface brightening[6] [rows] in the eight infrared methane windows [columns]. Red arrows point to the bright spots, the cloud and the surface bright spot. Whereas the methane cloud and the surface brightening (two bottom rows) are highly reflective and still detectable in all the methane windows, the T56, T65 and T70 bright spots (top three rows) are completely undistinguishable or only barely visible in windows at wavelengths shorter than 1.59-µm. Again, the three spots are observed with a more favorable geometry (with lower airmass) than the cloud and the surface bright spot, indicating that their disappearing at a shorter wavelength is not due to geometric effects. This peculiar behavior of the T56, T65 and T70 events denotes a strong positive spectral slope over the entire infrared range of VIMS that has never been observed at that magnitude for any methane clouds or surface brightening events. We attributed this peculiar spectral behavior to the presence of a cloud of suspended particle with a significant different altitude and/or composition than the methane clouds already observed in Titan's troposphere. Comprehensive radiative transfer calculations will allow us to determine their altitude and composition more accurately.

3. Radiative transfer model and VIMS data inversion scheme

3.1 Table S1. List of VIMS observations used in this study

	Date (flyby)	VIMS cube	Ls* (°)	Properties of the extracted pixel					
				Latitude	East long.	Res. (km)	Inc. (°)	Emerg. (°)	Phase (°)
T56 event	5/6/2009 (T54)	1620286756	356.8	-6.1	27.6	80	5.3	57.5	62.8
	5/22/2009 (T55)	1621675495	357.3	-1.9	25.6	113	3.1	51.5	53
	6/7/2009 (T56)	**1623062861**	**357.9**	**-2.4**	**24.7**	**142**	**4.4**	**41.8**	**44.1**
	10/12/2009 (T62)	1634064034	2.2	-5.0	27.3	94	6.9	8.4	10.7
T65 event	12/12/2009 (T63)	1639302760	4.3	-13.8	95.6	80	17.6	55.1	46.5
	12/28/2009 (T64)	1640670042	4.8	-13.7	95.4	46	19.4	54.3	45.3
	1/12/2010 (T65)	**1642062630**	**5.3**	**-13.9**	**96.0**	**85**	**17.9**	**51.1**	**44.2**
	1/28/2010 (T66)	1643438315	5.9	-14.2	96.8	75	18.4	51.3	43.9
T70 event	6/5/2010 (T69)	1654432101	10.2	-4.8	-175.2	96	70.7	40.3	30.3
	6/21/2010 (T70)	**1655801953**	**10.7**	**-5.2**	**-175.3**	**67**	**67.8**	**37.7**	**32**
	7/7/2010 (T71)	1657180617	11.2	-5.1	-175.4	69	67.6	33.6	34.2

* Solar longitude (Ls = 0° for northern spring equinox).

3.2 Description of the model

Our radiative transfer model is a slightly updated version of the one presented in detail in ref. (*19*). In our model, Titan's atmosphere is divided into 70 layers extending from the surface up to 700 km altitude. We include atmospheric opacity sources from gases (Rayleigh scattering from nitrogen and methane, collision-induced absorption by nitrogen and hydrogen, and absorption by methane, its isotopologues $^{13}CH_4$ and CH_3D, and carbon monoxide) and photochemical aerosols. Molecular linelists for gaseous methane and its isotopologues have been compiled over the whole spectral range of VIMS infrared channel (0.88-5.1 µm) from the most recent laboratory measurements, theoretical calculations and empirical models (all the corresponding references can be found in ref. (*19*)). Line lists for carbon monoxide are taken from the GEISA2009 database. Correlated-k absorption coefficients have been computed for all the gaseous species at the VIMS spectral sampling, on a "pressure-temperature-gas mole fraction" grid defined by Huygens and Cassini measurements. Concerning the aerosols, we use as a reference the phase function, single scattering albedo and vertical extinction profile measured *in situ* by the Huygens/DISR instrument[25], extrapolated in wavelengths to the VIMS infrared range. In order to account for the seasonal and latitudinal variability of the haze content, we allow the reference aerosol extinction profile to be freely multiplied by a uniform scaling factor. Given the current uncertainties on the optical properties of haze particles (extinction, phase function and single scattering albedo vs altitude), amplified by the application of empirical rules of extrapolation to the VIMS wavelength range, the scaling factor is generally constrained with 5 to 10% uncertainties at best. Given those uncertainties, we verified that the use of a uniform scaling factor does not alter nor degrade the outputs of the model and provide a robust descriptor of the seasonal and latitudinal variability of the haze population. In the more recent version of the code, we add the possibility to simulating a "cloud" of suspended particles in the lowest part of the atmosphere. The cloud is defined by four parameters: top altitude, effective radius of the constituting particles, optical depth at 2-µm and particle composition. The cloud particles are assumed to be spherical and their radii follow a log-normal distribution centered on the effective radius. The simulated cloud is alternatively composed of either liquid methane droplets (refractive indices taken from ref. (*41*)) or solid organic particles analogue to airborne photochemical aerosols, i.e. "tholins" particles (the refractive indices of tholins are taken from of ref. (*42*) - the imaginary part has been modified following the new calculations of ref. (*43*)). The assumption of sphericity for suspended solid organics is valid if the particles come from the surface where alteration and/or erosional processes are expected to naturally round them out. The single-scattering albedo and phase function of the cloud particles, along with the wavelength dependence of the optical depth of the cloud (the optical depth at 2-µm serving as a pivot) are calculated with the Mie theory. With these parameters determined, it is also possible to calculate the average number density of the cloud particles. Finally, a Lambertian surface is assumed. Given an input surface and an atmospheric model, the radiative transfer calculation is performed via the plane-parallel version of the Spherical Harmonic Discrete Ordinate Method solver (SHDOMPP).

This model can be used to invert VIMS infrared spectra of Titan. The six free parameters of our model are the multiplicative factor applied to the DISR haze extinction profile, the surface albedo and the composition, optical depth, top altitude and particle effective radius of a low altitude cloud. The haze extinction profile can be independently and unambiguously constrained at wavelengths exterior to the windows, where methane strongly absorbs photons, thus insensitive to altitudes lower than 70 km and most sensitive to the haze only. Once Titan's atmospheric haze opacity is constrained, we can then determine the surface albedo (and possibly properties of a low altitude cloud) by reproducing Titan's observed reflectivity in the windows.

3.3 Extraction of the atmospheric haze content from "before", "during" and "after" spectra and the surface albedo from "before" and "after" spectra

For our study, we extracted three "event" VIMS spectra from the brightest pixel of each of the bright spots. For each event, when available, "before/after" spectra over the same geographic location were also extracted from preceding and following flybys when no brightenings are seen. The acquisition periods of these spectra all fall within a five terrestrial month interval around the date of the brightening events (between the 6 May (T54) and 12 October 2009 (T62) for T56, 12 December 2009 (T63) and 28 January 2010 (T66) for T65, 5 June (T69) and 7 July 2010 (T71) for T70). From radiative transfer calculations with no cloud included, we derived Titan's haze extinction for all selected observations (**Table S2**) and surface albedos in the absence of the brightenings (**Fig. S4**). The retrieved "before/after" surface albedos for each of those areas are strikingly similar. Following our hypothesis that the brightenings are only atmosphere-related, this strongly suggests that surface albedos have not been modified during the whole considered time interval. As a consequence, we can in turn confidently use their respective average as input for the inversion of the "event" spectra.

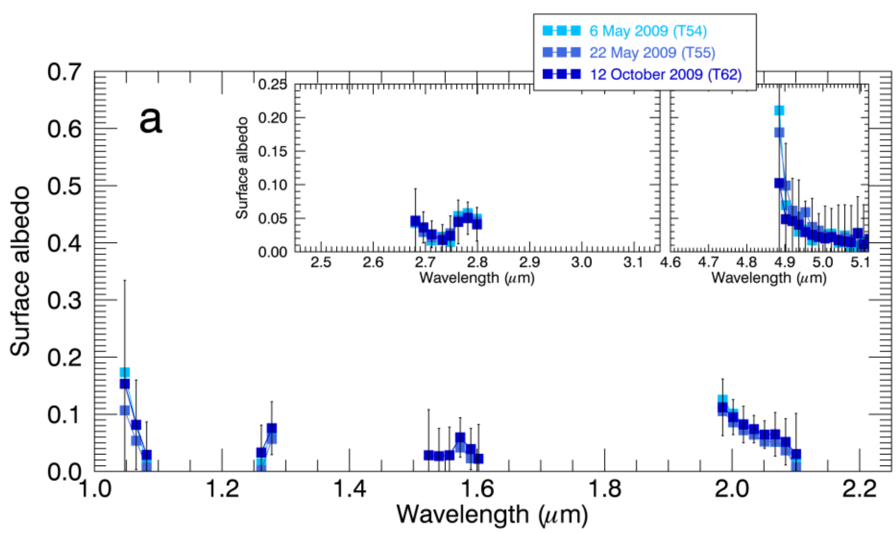

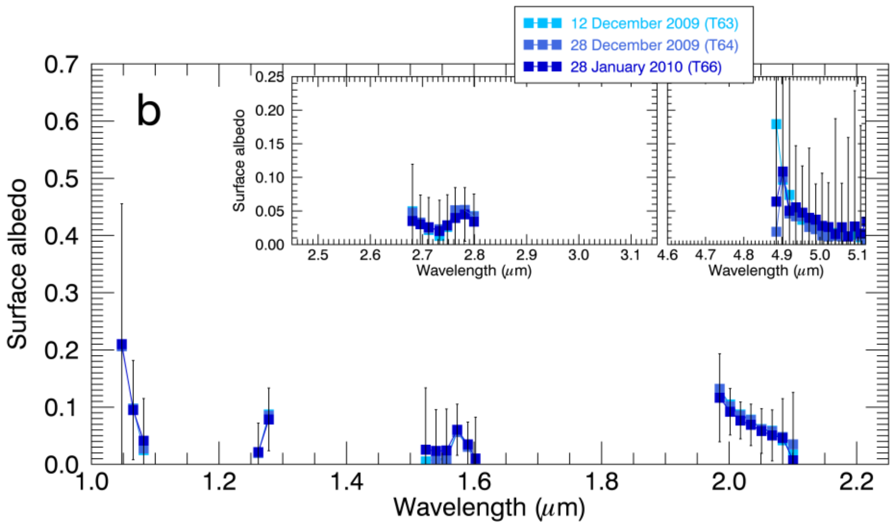

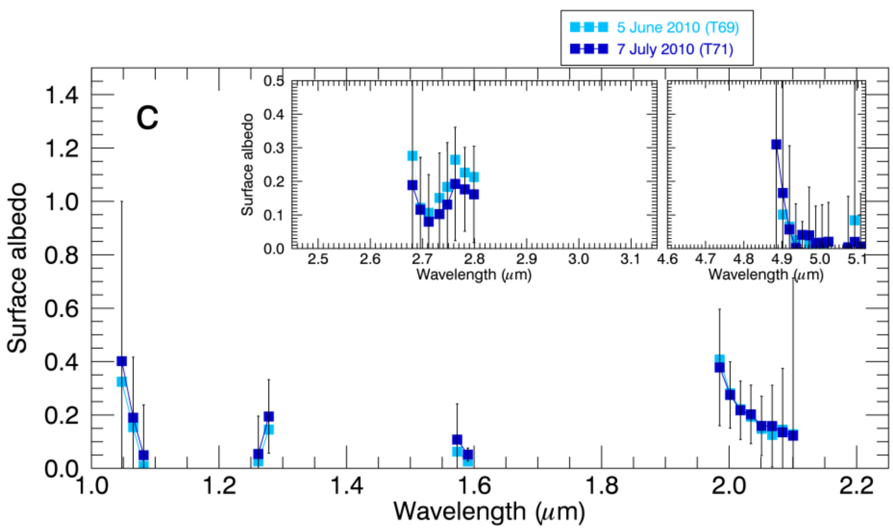

Fig. S4. Surface albedo of observations before and after the T56 (a), T65 (b) and T70 (c) events in the methane windows. We used the haze factors determined out of the methane windows (**Table S2**) as inputs for the determination of surface albedos. χ^2 goodness-of-fit estimators were calculated from the radiance factor I/F residuals in each of the methane windows, allowing us to isolate the best fits and to evaluate uncertainties on the retrievals. Those uncertainties include the cumulative influences of signal noise and errors on the haze population previously retrieved[19].

Table S2. Inversion of the haze total opacity for all the observations needed to analyze the spectra of the T56, T65 and T70 bright spots. We calculated the multiplicative factor to be applied to the DISR haze extinction profile in order to match the reflectivity of Titan's infrared spectra within the methane absorption bands. To measure how well the model agrees with the data at those selected wavelengths, we use the χ^2 merit function. The uncertainties on the values of the haze factor have been estimated to be ~5-10% (ref. *17*).

	T56 event				T65 event				T70 event		
Flyby	T54	T55	T56	T62	T63	T64	T65	T66	T69	T70	T71
Haze factor	0.75	0.8	0.86	1.0	0.76	0.78	0.82	0.7	0.92	0.94	0.94

3.4 Testing the surface "hot spot" hypothesis as an explanation for the T56, T65 and T70 brightenings

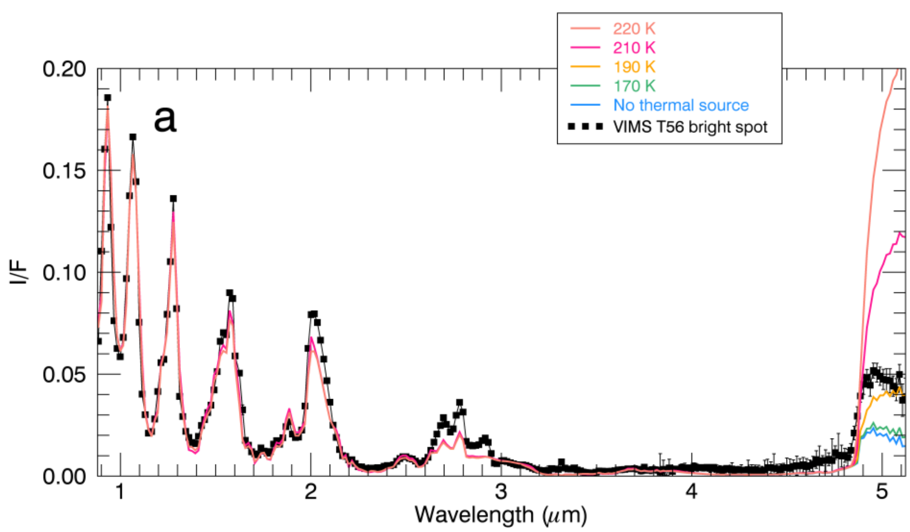

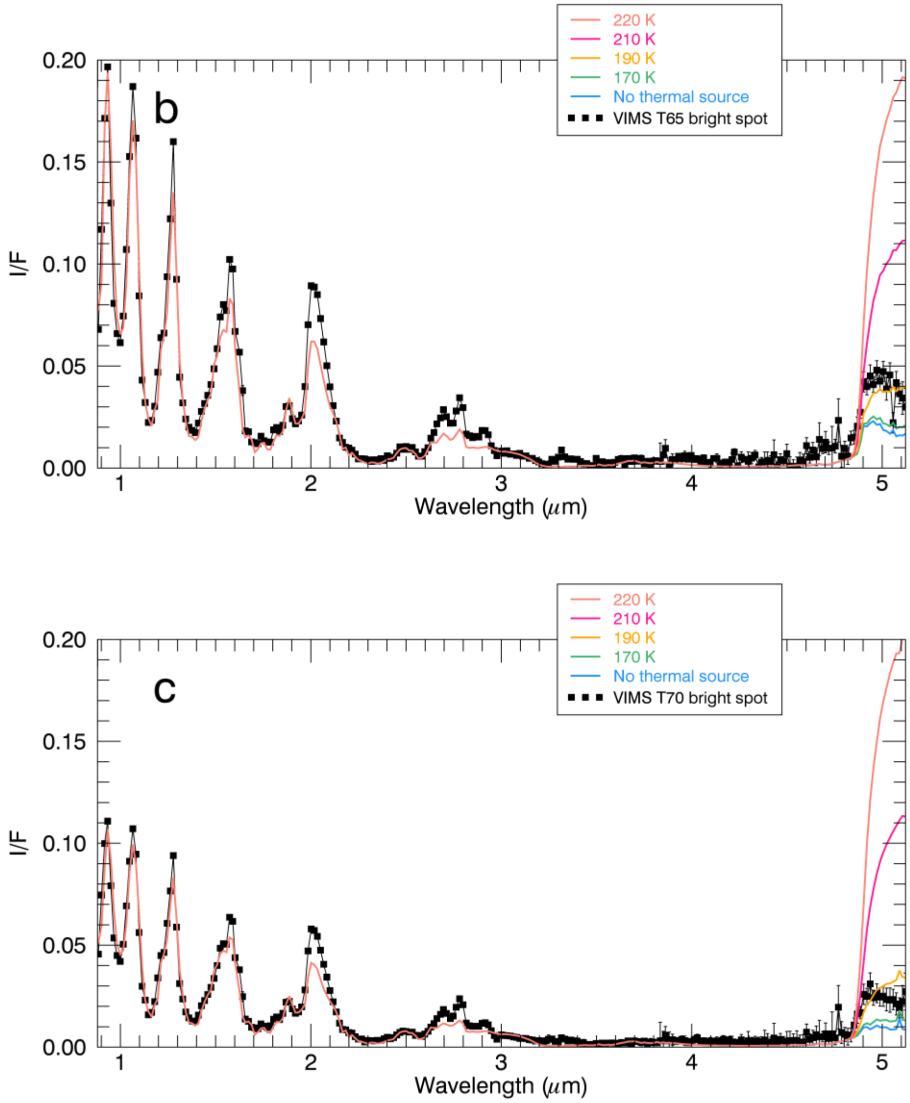

Fig. S5. Comparison between the spectra observed for the T56 (a), T65 (b) and T70 (c) bright spots (black squares) and spectra calculated with our radiative transfer model including a thermal source at the surface. Synthetic spectra over the entire VIMS infrared range are calculated for each of the three events using haze populations given in **Table S2** and average of the surface albedos retrieved from the "before" and "after" spectra above the same locations (see **Fig. S4**). In order to test the surface "hotspot" hypothesis, we also include in our calculations a source of surface thermal emission (with temperatures ranging from 100 to 250

K). We only show spectra calculated for temperatures of 170 (green), 190 (orange), 210 (deep pink) and 220 K (light pink). Below 170 K, there are no spectral differences between a "hot" surface and a surface without additional thermal source (light blue). The thermal emission affects the 5-µm atmospheric window only. The simulated spectrum with a surface at a temperature of 190 K provides the closest match to the observations in the 5-µm window. But even in this case, the calculated spectrum is far from reproducing the observed reflectance in the other atmospheric windows. The fact that no rise in surface temperature is able to explain the observed spectra makes the "hotspot" hypothesis hard to defend.

3.5 Inversions of the T56, T65 and T70 spectra including a cloud layer

Starting from the previous estimations of haze population and surface albedo (**Table S2** and **Fig. S4**), we search for the best match between the full radiative transfer model (including a "cloud" layer) and the three VIMS spectra extracted from the brightest pixels of the T56, T65 and T70 events. As we have to deal with a more extensive space of parameters to explore (the four cloud parameters: composition, top altitude 'z_{top}', optical depth at 2-µm 'τ' and effective radius of particles 'r_{eff}' of the cloud) than for the previous steps of the inversion, we choose at this stage to minimize the χ^2 merit function, built from the residuals between the observed and calculated spectra, by using a Levenberg-Marquardt algorithm, assisted by a genetic algorithm. Run first, the genetic algorithm allows us to narrow down the interval of variation of the four parameters. The restricted ranges are then used as initial guesses for the Levenberg-Marquardt algorithm that makes the final inversion more robust.

We used the classical reduced χ^2 function of merit:

$$\chi^2_{red} = \frac{1}{\nu}\sum_{i=1}^{N}\left(\frac{\frac{I}{F}_i^{obs} - \frac{I}{F}_i^{model}}{\sigma_i}\right)^2$$

with ν the number of degrees of freedom (ν = N – D – 1, with N the number of observations and D the number of estimated parameters), and σ_i the noise level of the data. The reduced χ^2 are estimated at wavelengths longward of the 1.27-µm atmospheric window, in a range where the T56, T65 and T70 bright spots show most of the spectral variability with respect to their surroundings. We also limit the calculation of the reduced χ^2 in the atmospheric windows, the only wavelengths spectrally sensitive to the surface and low atmosphere. Extending the calculation of the reduced χ^2 at shorter windows does not bring additional constraints to the inversion process. Therefore, we have in total N = 58 (all the VIMS spectral bands in the atmospheric windows from 1.4 to 5.12 µm).

Step 1. The genetic algorithm: finding a first estimation of the best fitting parameters.

To search for the miminum of the merit function within the space of our free parameters, we use as a first step the genetic algorithm (GA) available at http://www.ncnr.nist.gov/staff/dimeo/idl_programs.html (under the heading of ANALYSIS PROGRAMS)[44] (more information can be found at http://www.ncnr.nist.gov/dave). As our full radiative transfer model is heavily time-consuming, the advanced stochastic and directed strategy of the GAs ensures a reasonable number of calls to the model, but still with a limited risk of getting stuck in local minima. The GA functions iteratively as follows: (1) an initial population of "NPOP" members (chromosomes) is created, each chromosomes being encoded in binary, made up of the concatenation of the individual parameters (genes) of a chosen number of bits "GENE_LENGTH", (2) the fitness of each member of the initial population is calculated, (3) a new population of members is created based on the fitness of the members of the previous population, (4) members of the new population are selected at random and genetically mixed in an operation called crossover with a probability “PCROSS”, (5) a random gene within a randomly selected chromosome is modified in mutation with the probability “PMUTATE”, and (6) return to step (2) and iterate until either a fixed convergence criterion has been satisfied or maximum number of iterations (generations) have been performed.

Starting from an initial population NPOP=100 (sufficient to guarantee enough variability in the [z_{top}, τ, r_{eff}] parameter population), with GENE_LENGTH=10 (enough numerical precision of the result), PCROSS=0.9 and PMUTATE=0.25, we ran the GA twenty times per brightening event, i.e. ten times for each of the two cloud particle compositions (liquid methane and tholins). The parameters are restricted to vary within the range [0-60] km for z_{top}, [0.01-20] for τ and [0.1-50] µm for r_{eff}. Each run of the genetic algorithm takes ~72 hours for 1,100 calls to the radiative transfer model. The estimated 10 best sets of parameters for the 2 cloud compositions are shown for the T56, T65 and T70 spectra in **Table S3**. Those runs allowed us to explore the region close to the minimum of reduced χ^2 and to check for the absence of inter-correlation between the retrieved parameters. Particle radius and total cloud opacity are both clustered in narrow regions of the parameter space, indicating, at least qualitatively, that the inversions are robust for those two parameters. Top altitudes are more widely distributed, revealing a weaker constraint on this parameter.

Table S3. Summary of all individual inversion runs using the genetic algorithm.

T56			T65			T70		
r_{eff} (µm)	τ	z_{top} (km)	r_{eff} (µm)	τ	z_{top} (km)	r_{eff} (µm)	τ	z_{top} (km)
Liquid methane								
5.3	0.59	15.6	18.8	0.56	13.5	5.3	1.24	8.8
5.0	0.74	9.2	4.2	0.48	15.0	5.1	1.07	10.4
5.2	0.70	8.7	4.8	0.66	15.0	5.3	1.03	10.7
6.4	0.56	12.2	4.7	0.76	7.9	5.2	0.89	13.7
5.3	0.66	9.8	4.8	0.85	8.6	4.7	0.79	16.7
6.3	0.67	11.5	4.9	0.66	13.4	5.3	1.15	13.7
5.5	0.77	8.6	4.8	0.68	13.6	6.2	1.19	12.6
5.5	0.64	12.2	4.7	0.76	7.9	4.9	1.34	7.2
6.2	0.64	12.5	4.9	0.69	12.6	5.2	0.90	16.6
5.4	0.63	12.1	4.8	0.65	13.8	5.1	1.10	12.3
Solid organics								
2.2	0.36	10.0	1.9	0.37	2.2	2.1	0.30	17.0
2.2	0.37	7.6	1.8	0.31	12.5	1.8	0.43	10.3
2.2	0.39	9.5	2.2	0.31	12.8	2.3	0.45	11.5
2.3	0.35	13.9	1.6	0.41	7.62	1.9	0.49	8.5
2.4	0.37	13.2	2.2	0.33	15.1	1.9	0.31	15.8
2.3	0.38	13.6	1.7	0.40	5.4	1.9	0.36	10.9
2.2	0.39	5.7	2.2	0.38	12.1	2.0	0.33	14.3
2.3	0.37	9.5	2.3	0.46	8.6	2.1	0.45	10.6
2.2	0.35	9.1	1.7	0.35	8.3	1.8	0.32	13.5
2.3	0.35	10.9	2.2	0.31	14.5	2.1	0.45	10.5

Step 2. The Levenberg-Marquardt least-square minimization: final inversions and evaluation of the statistics on the best fitting parameters.

The GA is well designed to avoid local minima of χ^2, but is not able to evaluate the statistics of the inversions by itself. On its side, the Levenberg-Marquardt algorithm (LMA)[45] is very complementary to the GA: it is well designed to provide the inversion statistics (i.e. via the calculation of the covariance of the standard errors in the fitted parameters), but can easily be trapped in local minima in the case of a χ^2 valley of tortured topography, being very sensitive to the initial guess for the set of fitted parameters.

We thus use the GA outputs (see **Table S3**) to feed the LMA with robust initial guesses. The final inversion is done with the LMA, with four fitted parameters for the cloud layer: z_{top} free to vary in the [1-60] km range, τ in the [0.01-20] range, r_{eff} in the [0.1-50] mic. range, as for the GA runs, and "composition" parameter in the [0-1] range, with liquid methane for values of the parameter lower than 0.5 and tholins for values greater than 0.5.

The ranges for the LMA starting guesses are the following:

(1) T56: [5-16] km for z_{top}, [0.3-0.8] for τ, [2-7] μm for r_{eff}, and liquid methane for the composition.

(2) T65: [2-16] km for z_{top}, [0.3-0.9] for τ and [1.5-5] μm for r_{eff}, and liquid methane for the composition.

(3) T70: [7-17] km for z_{top}, [0.2-1.4] for τ and [1-7] μm for r_{eff}, and liquid methane for the composition.

The LMA is then run 40 times, for each bright spot spectrum, in order to explore as many combinations of starting guesses as possible within the ranges given by the GA, the composition being systematically started as liquid methane. For most of the inversion runs, the convergence criterion (absolute difference in χ^2 less than 10^{-3} between two successive iterations) is rapidly met after less than 150 calls to the model.

The outputs of the 40 runs realized for each of the three events' spectra are shown in **Table S4**. The table compiles the final values for the for cloud parameters: composition, r_{eff}, τ and z_{top}, along with their corresponding uncertainties. The runs are ordered by increasing reduced χ^2.

Table S4. List of the LMA outputs for the 40 runs of the T56 spectrum inversion. The best fit for a tholin cloud is outlined in green and for a liquid methane cloud in blue.

χ^2_{red} (>1.4 μm)	Comp.	r_{eff} (mic.)	Δr (mic.)	τ	$\Delta\tau$	z_{top} (km)	Δz (km)
11.7340	THOLINS	2.48517	0.172634	0.470960	0.0380395	13.9413	1.61866
11.7796	THOLINS	2.48641	0.171785	0.471647	0.0378433	13.9227	1.62606
11.8368	THOLINS	2.48699	0.172140	0.473165	0.0380089	13.8721	1.62497
12.0511	THOLINS	2.49037	0.171160	0.474158	0.0375478	13.9665	1.61610
16.5171	THOLINS	2.73579	0.264037	0.591750	0.0732123	14.4969	1.85070
16.5524	CH4	4.00142	1.78389	0.501467	0.316223	10.5206	2.02830
16.5703	CH4	3.97758	2.50885	0.506700	0.451679	9.59287	2.14770
17.8220	THOLINS	2.75300	0.253592	0.612630	0.0741527	14.4326	1.75448
17.9236	CH4	4.02208	1.26344	0.496883	0.220765	12.3644	2.05294
20.3682	THOLINS	5.75456	0.523206	0.609200	0.0387605	15.8564	2.19254
20.3682	THOLINS	5.75456	0.523206	0.609200	0.0387605	15.8564	2.19254
20.9003	CH4	4.02972	1.45512	0.594372	0.303869	8.58274	2.22318
20.9116	THOLINS	5.76507	0.548735	0.623794	0.0383751	15.1551	2.01771
21.5088	THOLINS	5.78127	0.550663	0.634865	0.0379741	14.5549	1.83355
21.7559	THOLINS	5.73333	0.519188	0.640187	0.0394346	15.2579	2.02297
22.3941	THOLINS	5.76481	0.495439	0.626796	0.0381553	15.8311	2.10435
22.4520	THOLINS	6.10995	0.616705	0.655025	0.0402820	15.5560	2.16712
22.5062	THOLINS	6.42622	0.679961	0.617590	0.0417620	16.1232	2.12680
22.6742	THOLINS	6.12333	0.622819	0.654808	0.0403968	15.5777	2.16509
22.7022	THOLINS	6.41786	0.661513	0.627460	0.0416413	15.9473	2.15859
23.1743	THOLINS	6.39448	0.610599	0.679642	0.0414120	13.5838	1.69337
23.2630	THOLINS	6.40723	0.640654	0.678613	0.0417800	13.5981	1.70889
23.3960	THOLINS	5.52688	0.579730	0.612727	0.0387499	15.7692	2.12226
23.4076	THOLINS	6.14881	0.579093	0.693108	0.0386960	14.0103	1.67523
23.4500	THOLINS	6.14130	0.581308	0.659804	0.0399208	15.6607	2.17488
23.4500	THOLINS	6.14130	0.581308	0.659804	0.0399208	15.6607	2.17488
23.5476	THOLINS	6.73277	0.799957	0.628493	0.0387963	15.3609	2.04311
23.6135	THOLINS	6.42054	0.647748	0.641480	0.0419165	15.4195	2.06486
23.7741	THOLINS	5.51491	0.606557	0.615119	0.0385539	15.7997	2.09250
24.2185	THOLINS	5.77124	0.534140	0.640424	0.0388604	15.6947	2.11838
24.3077	THOLINS	6.38869	0.617538	0.657261	0.0418250	15.2462	1.98907
24.3273	THOLINS	6.43224	0.639717	0.651150	0.0420550	15.2169	1.98641
24.4082	THOLINS	7.41930	0.641476	0.656069	0.0388688	15.7628	2.16128
24.5799	THOLINS	6.40880	0.594712	0.644314	0.0400805	16.0809	2.03475
24.6228	THOLINS	6.40267	0.622526	0.646155	0.0408665	15.9128	2.09995
24.6875	THOLINS	7.05102	1.07243	0.632994	0.0388554	15.5780	2.24873
24.8376	THOLINS	6.36512	0.625493	0.644559	0.0406146	15.8988	2.16971
24.9980	THOLINS	7.09379	0.890253	0.653960	0.0389093	15.0235	2.01190
25.1409	THOLINS	7.07156	0.964836	0.641778	0.0430508	15.6306	2.30480
25.3138	THOLINS	5.44969	0.663600	0.603895	0.0466858	15.4368	1.97952

Table S4 (continued). Same as previous, for the T65 spectrum inversion. The best fit for a tholin cloud is outlined in green and for a liquid methane cloud in blue.

χ^2_{red} (>1.4 μm)	Comp.	r_{eff} (mic.)	Δr (mic.)	τ	$\Delta\tau$	z_{top} (km)	Δz (km)
1.11652	THOLINS	2.23792	0.198502	0.442653	0.0840744	9.71752	1.87488
1.15278	THOLINS	2.19534	0.184667	0.398186	0.0773023	11.0381	1.85915
1.35956	THOLINS	1.55802	0.0508493	0.405784	0.0289176	11.8535	1.84282
1.39775	CH4	4.45419	0.326825	0.741006	0.0783070	10.4202	1.51055
1.40124	CH4	4.31349	0.506072	0.778004	0.149613	6.30735	2.29811
1.41233	THOLINS	1.83011	0.317504	0.368071	0.0499658	8.35607	2.18862
1.48926	CH4	3.77952	1.54647	0.510567	0.236667	13.0358	1.84947
1.49550	CH4	3.59999	1.01577	0.540000	0.0662373	10.4000	1.95813
1.53681	THOLINS	2.51546	0.219145	0.509222	0.0519210	15.3874	2.67384
1.54062	CH4	3.60000	1.42583	0.540000	0.0965108	7.60000	2.98159
1.67132	THOLINS	2.49863	0.241220	0.623806	0.0671360	10.2545	2.00700
1.82105	THOLINS	2.53470	0.209196	0.607134	0.0492203	13.9815	1.98510
1.82136	THOLINS	2.50278	0.254076	0.684442	0.0763089	8.15868	2.08899
1.82469	CH4	3.60000	0.926880	0.660000	0.0771179	7.60001	1.83302
1.82485	THOLINS	4.80496	0.481605	0.624855	0.0423944	16.1830	2.17630
1.83461	THOLINS	2.96909	0.275298	0.643375	0.101395	11.0778	2.72943
1.83501	CH4	3.99860	1.70199	0.707898	0.435877	6.25383	2.07264
1.87543	THOLINS	4.81660	0.484889	0.652560	0.0446147	15.1648	2.08033
1.96684	CH4	3.54938	1.20083	0.582390	0.0408353	12.4144	1.70421
1.99905	THOLINS	4.92857	0.524162	0.624416	0.0508373	15.4558	2.29505
2.01418	THOLINS	4.94414	0.548081	0.638450	0.0535762	14.9289	2.05869
2.06184	THOLINS	2.56930	0.203375	0.665040	0.0499771	13.7239	2.07801
2.22882	THOLINS	4.77071	0.418144	0.676124	0.0472546	15.2942	2.06723
2.26427	THOLINS	3.00318	0.238215	0.686431	0.102023	11.7975	2.89543
2.26458	THOLINS	4.95194	0.509614	0.657242	0.0555890	15.4198	2.08309
2.28481	THOLINS	4.77067	0.421437	0.681296	0.0474662	15.2616	2.05192
2.30502	CH4	3.58848	0.862463	0.654992	0.0541275	10.3761	1.40023
2.38399	THOLINS	3.06286	0.254254	0.701640	0.0957595	10.2586	2.86937
2.47416	THOLINS	5.48216	0.642036	0.690511	0.0499982	14.3850	1.90236
2.70382	THOLINS	2.61196	0.251824	0.796585	0.0684716	9.88102	2.06196
2.85209	THOLINS	3.40490	0.329940	0.625344	0.0710412	10.4859	2.52252
2.85209	THOLINS	3.40490	0.329940	0.625344	0.0710412	10.4859	2.52252
2.85209	THOLINS	3.40490	0.329940	0.625344	0.0710412	10.4859	2.52252
2.85209	THOLINS	3.40490	0.329940	0.625344	0.0710412	10.4859	2.52252
3.08033	CH4	2.19568	3.40782	0.974554	4.35651	8.71916	8.32858
3.16582	CH4	2.32346	2.09860	0.871002	1.99888	8.17313	9.64081
3.29398	CH4	1.91793	3.54358	1.02164	1.00522	8.79675	9.81517
3.41497	CH4	1.87535	1.48008	1.03677	0.339319	19.7871	5.09365
3.53140	CH4	2.20920	0.981724	1.00327	1.36631	19.2191	3.73571
3.63994	THOLINS	23.4026	8.71678	0.633844	0.0525946	15.4631	2.08295

Table S4 (continued). Same as previous, for the T70 spectrum inversion. The best fit for a tholin cloud is outlined in green and for a liquid methane cloud in blue.

χ^2_{red} (>1.4 µm)	Comp.	r_{eff} (mic.)	Δr (mic.)	τ	Δτ	z_{top} (km)	Δz (km)
3,11605	THOLINS	1,9493	0,198529	0,391077	0,117373	11,8339	2,79507
3,18485	THOLINS	1,94346	0,206665	0,412776	0,122852	10,9159	2,36104
3,20448	THOLINS	1,93235	0,197064	0,33475	0,0902277	14,7401	2,8154
3,45986	CH4	5,04931	2,12777	1,06378	0,455302	13,2517	2,58873
3,48156	CH4	5,24025	1,75441	1,18433	0,36649	11,613	3,00674
3,48542	CH4	5,04218	1,24619	0,953042	0,179357	14,7848	2,73323
3,50151	CH4	5,5448	0,777119	1,15387	0,210686	14,0918	2,24688
3,56868	CH4	5,52088	0,939854	1,34232	0,363427	11,4632	2,78622
3,57196	CH4	5,54514	0,8308	1,28837	0,313611	12,7437	2,48913
3,72952	THOLINS	1,92132	0,125345	0,368623	0,0693405	15,5319	2,31351
3,79669	THOLINS	1,88589	0,162476	0,446384	0,0901634	11,9018	2,03206
3,83031	CH4	5,80934	0,54088	1,18265	0,245582	14,3799	2,3318
4,52603	THOLINS	1,70566	0,121727	0,204803	0,0346775	29,6832	5,08098
4,58503	CH4	10,9911	3,25855	0,922653	0,231437	14,6571	3,13175
4,6001	CH4	10,9869	3,22542	0,925188	0,299297	14,6932	3,30188
4,63578	CH4	11,4705	3,90165	0,963747	0,361818	13,466	2,91585
4,63667	CH4	11,043	3,18303	1,02945	0,359382	13,3866	2,79613
4,67798	CH4	11,2539	3,44034	0,912502	0,337228	15,2329	3,73533
4,72111	CH4	11,3606	4,13879	1,03149	0,362732	13,4763	2,78713
4,72765	CH4	10,6154	3,64777	0,988289	0,210375	14,1439	2,68715
4,80198	CH4	17,5761	7,90015	0,790854	0,178751	13,9588	2,87451
4,81735	CH4	10,9815	3,11135	0,89303	0,265322	16,7018	3,28198
4,85086	CH4	17,0799	6,40769	0,757598	0,168776	14,1673	3,11027
4,8856	CH4	16,8435	6,29991	0,756572	0,169484	14,5229	3,33133
4,94937	CH4	47,9891	36,8913	0,775164	0,200951	14,8224	3,9842
4,97716	CH4	47,5187	35,4135	0,72539	0,148697	16,4523	4,18254
4,99799	CH4	49,1958	37,682	0,892356	0,192494	13,0545	3,19323
5,03118	CH4	10,6391	3,47142	0,88325	0,240761	17,7397	2,85873
5,09681	CH4	13,5516	5,49166	1,04267	0,384104	10,3796	3,10266
5,11424	CH4	23,5226	20,4807	0,935947	0,356481	13,226	3,30231
5,11863	CH4	19,7681	14,9441	1,086	0,667613	10,3242	3,06089
5,15224	THOLINS	1,69751	0,0923821	0,505389	0,0504532	13,2474	1,44
5,20999	CH4	4,97514	1,20542	1,51233	0,404783	11,7497	1,63598
5,22818	CH4	17,4889	14,8477	1,1091	0,872675	9,1511	3,19681
5,34244	THOLINS	1,7017	0,0880957	0,501447	0,0482068	13,7128	1,37285
5,52358	THOLINS	4,07955	1,38112	0,601165	0,136758	15,0483	4,67797
5,54515	THOLINS	7,34157	2,81127	0,701509	0,152024	14,3796	3,86246
5,58303	THOLINS	6,74714	2,51045	0,702915	0,143093	13,8755	3,53394
5,62864	THOLINS	7,28671	2,6627	0,773025	0,162158	13,4815	3,41825
5,65552	THOLINS	4,81107	0,840116	0,605245	0,132827	16,2158	4,82722

Overall, for all the brightening events, the best fits are all slightly improved with the LMA (with respect to the runs with the GA). In all cases, a cloud composed of tholins provides a better fit to the data than a liquid methane cloud, with χ^2_{red} = 11.7 against 16.6 for T56, χ^2_{red} = 1.1 against 1.4 for T65, and χ^2_{red} = 3.1 against 3.5 for T70 (**Table S4**). The best fits between the data and models are shown for the two compositions in **Figure 3** and the best retrieved composition, top altitudes, opacities and effective radii, and associated standard errors, are summarized in **Table S5** (the best values for the second type of composition are also indicated, though providing a poorer fit to the data). It is worth noting that, even if the inversion is calculated by using wavelengths greater than 1.4 µm, we check the quality of the fits at shorter wavelengths. The fits are still excellent over the full infrared range of VIMS (0.88-5.12 µm) (**Figure 2**). The best fits (and the corresponding best fitted parameters shown in **Table S4** and **S5**) stay unchanged if we calculate the reduced χ^2 over the entire range of VIMS. This confirms that, as observed, the 0.93, 1.08 and 1.27-µm windows are not sensitive to the spectral characteristics of those specific events and that the shortest windows do not bring any additional constraints to the inversion process.

Table S5. Best fits between the T56, T65 and T70 bright spot spectra and the radiative transfer model including a low-altitude cloud of suspended particles (tholins or liquid methane). This table shows the properties of the modelled “clouds” (composition, top altitude, optical depth at 2 µm and effective diameter of cloud particles with their uncertainties) that provided the best fit to the observed spectra (outlined in green). The best values for the second type of composition, though providing a poorer fit to the data, are also indicated. Incidence (i), emission (e) and phase (α) angles, as well as exposure time, are specified for each of the T56, T65 and T70 extracted spectra.

	Composition	Top altitude	Total opacity at 2 μm	Mean effective radius	Reduced-χ^2 (>1.4 μm)
T56 (i=4.4°, e= 41.8°, α=44.1°, 320 ms)	**Tholins**	**14 ± 2 km**	**0.5 ± 0.05**	**2.5 ± 0.2 mic.**	**11.73**
	Liquid CH_4	*10.5 ± 2 km*	*0.5 ± 0.3*	*4 ± 2 mic.*	*16.55*
T65 (i=17.9°, e=51.1°, α=44.2°, 80 ms)	**Tholins**	**10 ± 2 km**	**0.5 ± 0.1**	**2.5 ± 0.2 mic.**	**1.12**
	Liquid CH_4	*10.5 ± 1.5 km*	*0.75 ± 0.1*	*4.5 ± 0.5 mic.*	*1.4*
T70 (i=67.8°, e=37.7°, α=32°, 180 ms)	**Tholins**	**12 ± 3 km**	**0.4 ± 0.1**	**2 ± 0.2 mic.**	**3.12**
	Liquid CH_4	*13 ± 3 km*	*1.05 ± 0.5*	*5 ± 2 mic.*	*3.46*

3.5.1 Sensitivity tests for the model parameters close to their values providing the best fit

Besides the inversion calculations, we performed sensitivity tests of the model outputs to the cloud altitude and opacity, by varying one parameter at a time around its value providing the best fit, exploring a few other altitudes [25, 35 km] and opacities [0.1, 1, 2] for the two compositions. All the test results are presented in **Figure S6**.

336

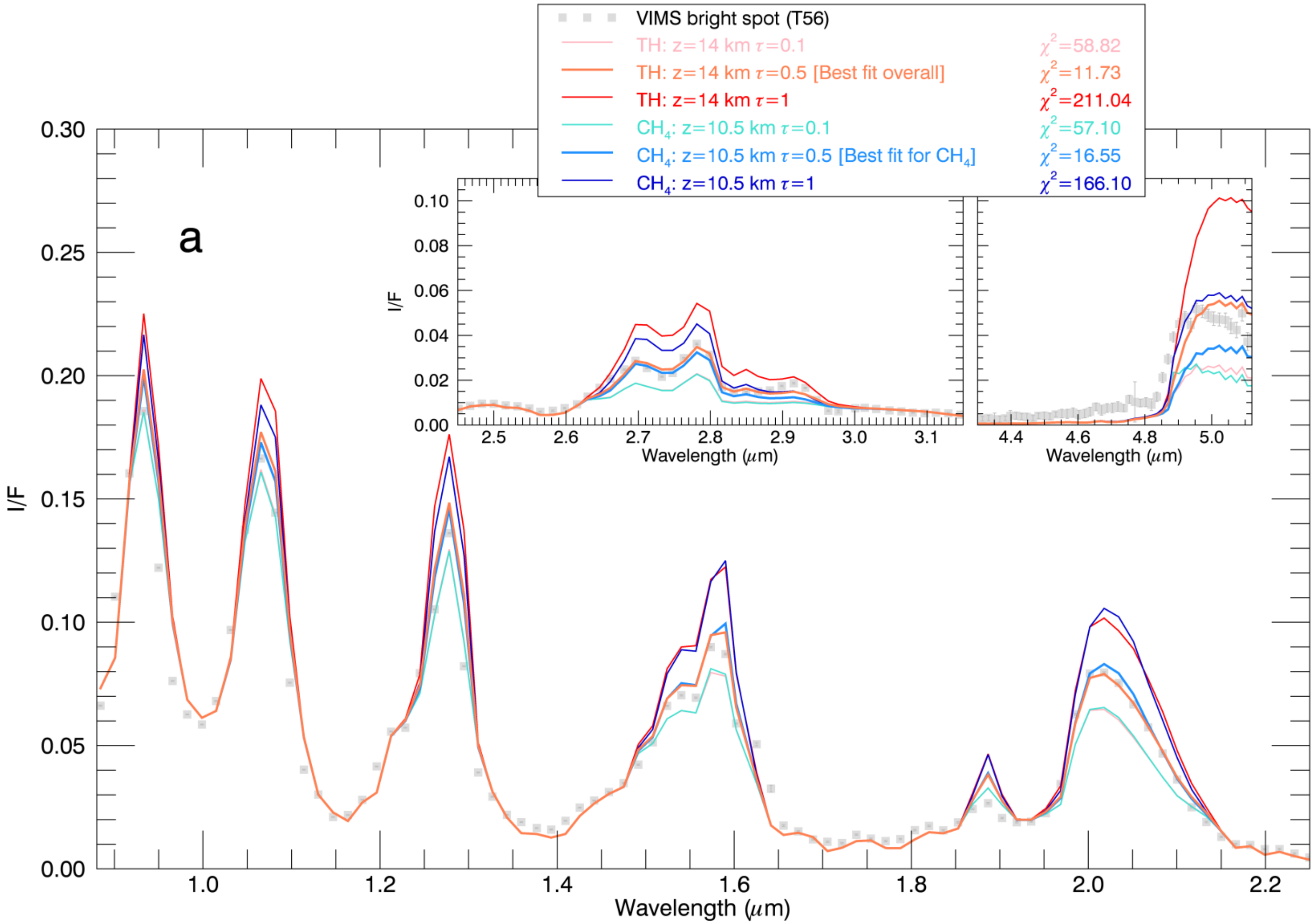
VIMS bright spot (T56)
TH: z=14 km τ=0.1
χ²=58.82
TH: z=14 km τ=0.5 [Best fit overall]
χ²=11.73
TH: z=14 km τ=1
χ²=211.04
CH₄: z=10.5 km τ=0.1
χ²=57.10
CH₄: z=10.5 km τ=0.5 [Best fit for CH₄]
χ²=16.55
CH₄: z=10.5 km τ=1
χ²=166.10
a
I/F
Wavelength (μm)
0.30
0.25
0.20
0.15
0.10
0.05
0.00
1.0
1.2
1.4
1.6
1.8
2.0
2.2
0.10
0.08
0.06
0.04
0.02
0.00
2.5
2.6
2.7
2.8
2.9
3.0
3.1
4.4
4.6
4.8
5.0

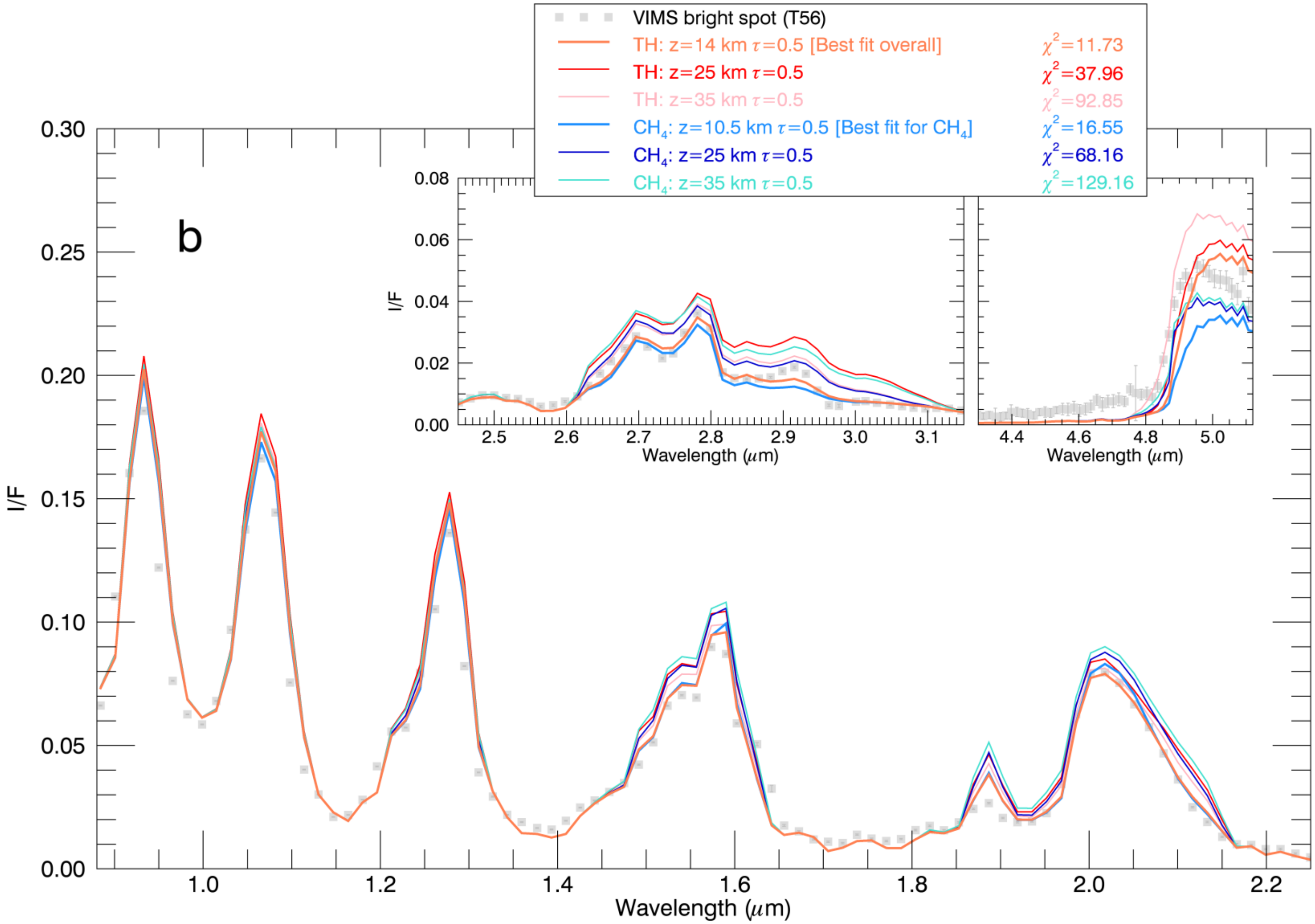

b
VIMS bright spot (T56)
TH: z=14 km τ=0.5 [Best fit overall] χ2=11.73
TH: z=25 km τ=0.5 χ2=37.96
TH: z=35 km τ=0.5 χ2=92.85
CH4: z=10.5 km τ=0.5 [Best fit for CH4] χ2=16.55
CH4: z=25 km τ=0.5 χ2=68.16
CH4: z=35 km τ=0.5 χ2=129.16
I/F
Wavelength (μm)

337

Figure S6. (**a) and (b)**. T56 observations (gray squares), including 1σ error due to noise in VIMS spectrum, are compared to models (solid lines). The models are calculated with a cloud layer at best fitted altitudes (here 14 km for tholins and 10.5 km for liquid methane) for several optical depths **(a)** and at best fitted optical depths (here 0.5 for tholins and liquid methane) for several altitudes **(b)**, and compared with the best fits for tholins and liquid methane composition. Resulting reduced χ^2 are indicated. The overall best fit is provided by a cloud composed of tholins with a significant statistical difference. The model is substantially more sensitive to variation in cloud optical depth than in cloud altitude, revealing a weaker constraint on this latter parameter.

344

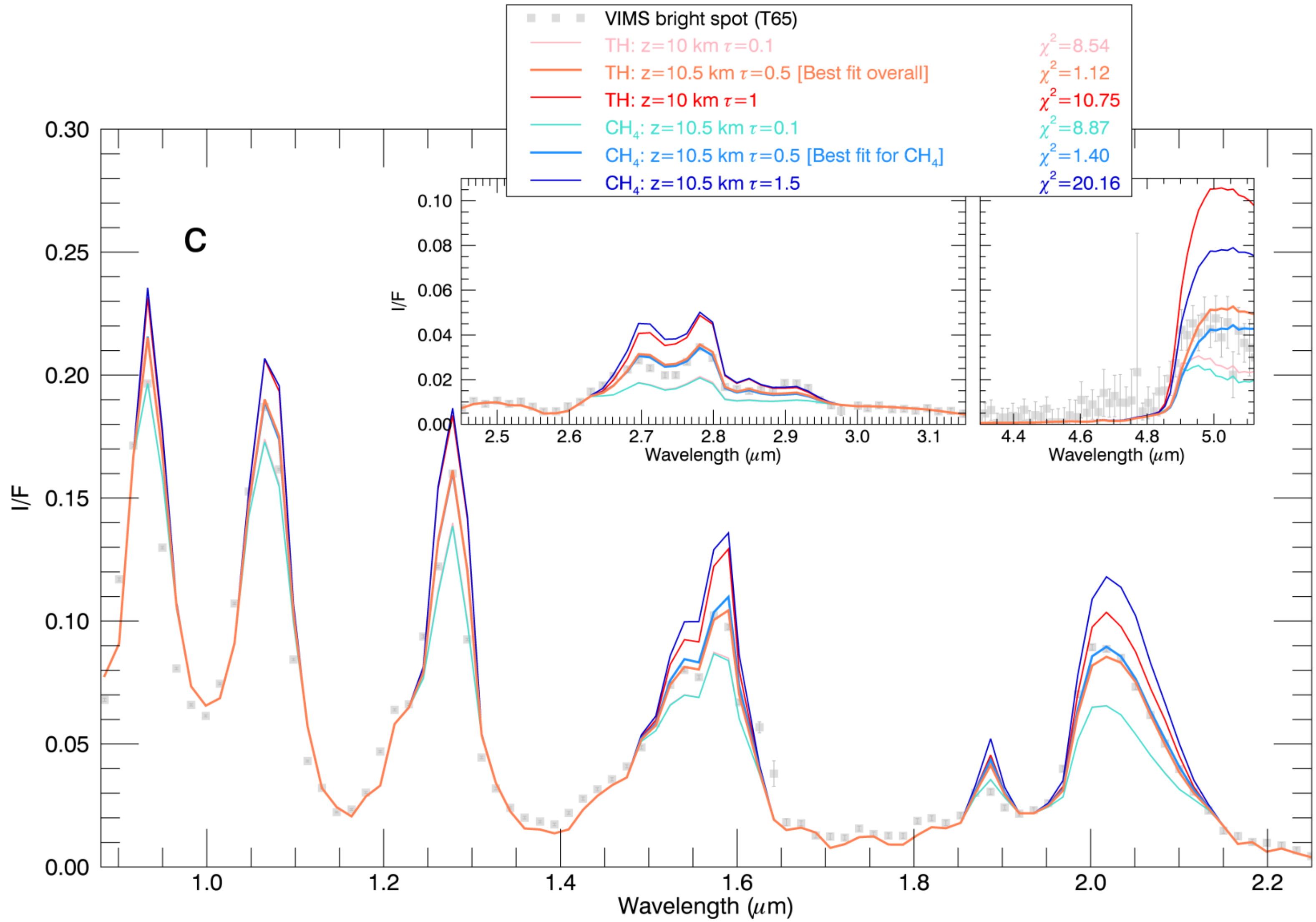

VIMS bright spot (T65)
TH: z=10 km τ=0.1 χ^2=8.54
TH: z=10.5 km τ=0.5 [Best fit overall] χ^2=1.12
TH: z=10 km τ=1 χ^2=10.75
CH_4: z=10.5 km τ=0.1 χ^2=8.87
CH_4: z=10.5 km τ=0.5 [Best fit for CH_4] χ^2=1.40
CH_4: z=10.5 km τ=1.5 χ^2=20.16
C
I/F
Wavelength (μm)

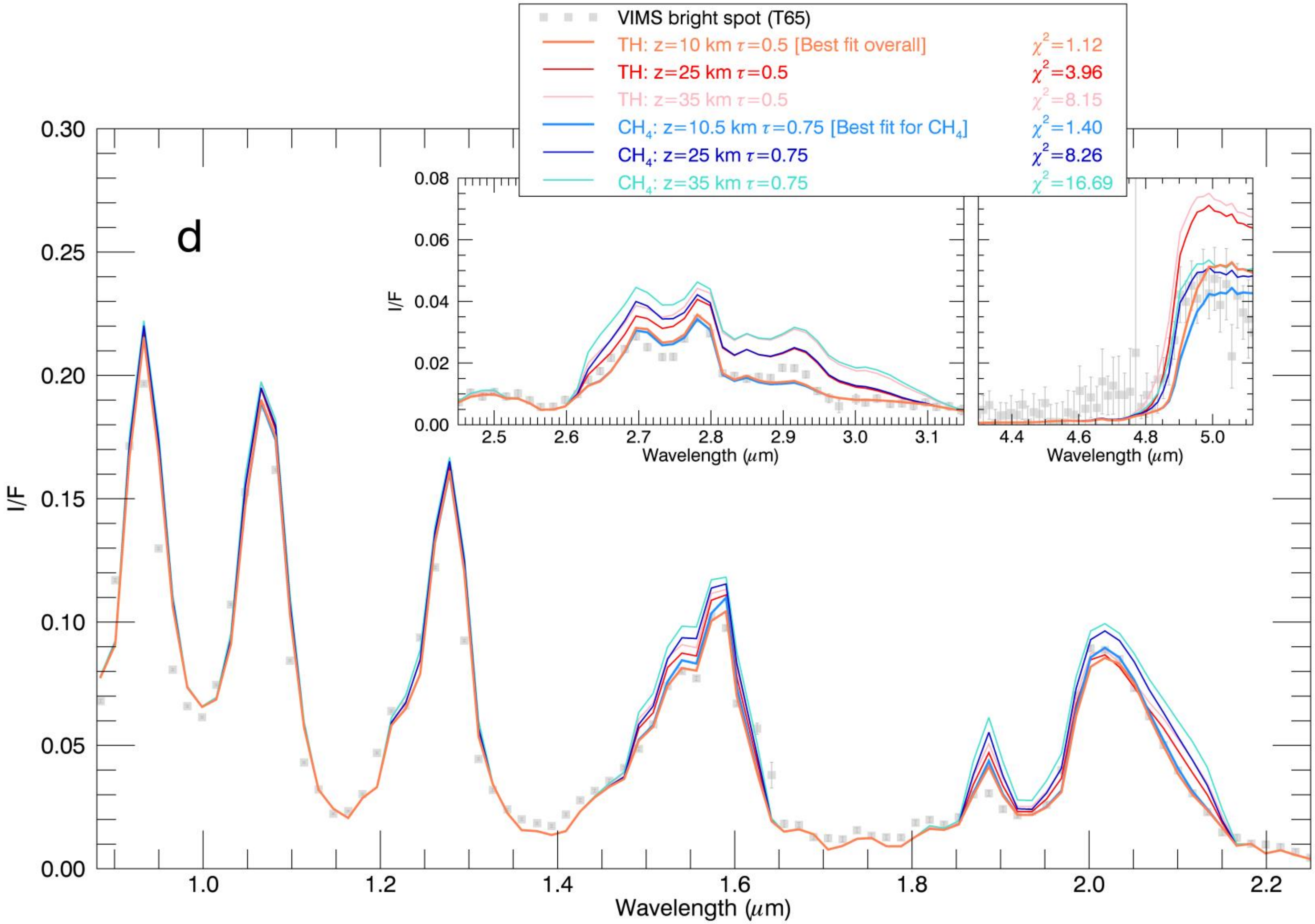

Figure S6 (continued). (c) and (d) Same for T65 observations.

347

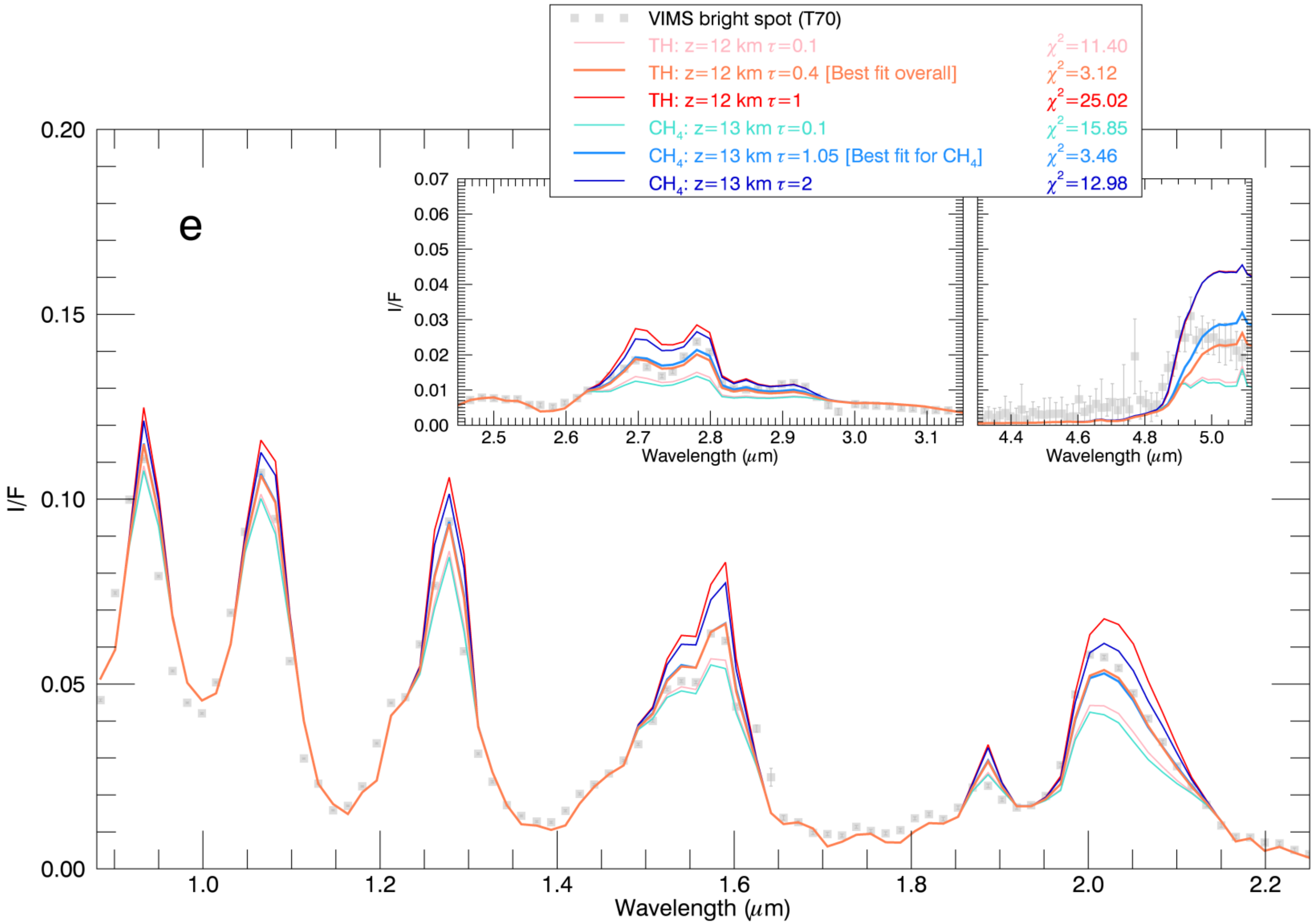

VIMS bright spot (T70)
TH: z=12 km τ=0.1 χ²=11.40
TH: z=12 km τ=0.4 [Best fit overall] χ²=3.12
TH: z=12 km τ=1 χ²=25.02
CH₄: z=13 km τ=0.1 χ²=15.85
CH₄: z=13 km τ=1.05 [Best fit for CH₄] χ²=3.46
CH₄: z=13 km τ=2 χ²=12.98
e
I/F
Wavelength (μm)

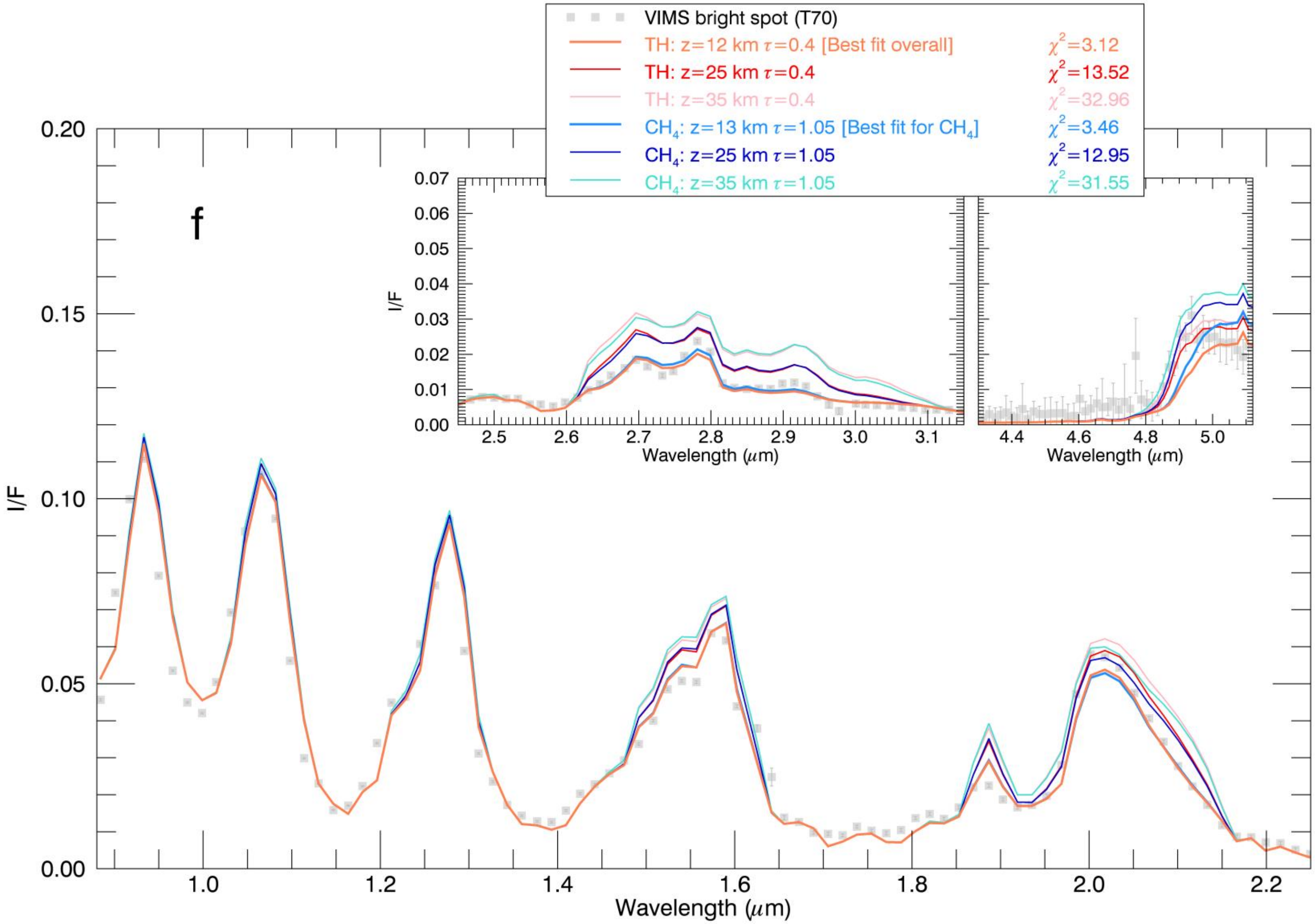

Figure S6 (continued). (e) and (f) Same for T70 observations.

3.5.2 Ability of our model to distinguish between methane and solid organic clouds

We also performed a test that allowed us to validate the ability of our radiative transfer model to distinguish between a cloud composed of solid organic particles (tholins) or liquid methane droplets. For this purpose, we used a spectrum extracted from the VIMS observation of a methane cloud acquired on 26 October 2004 (TB flyby). This cloud, already analyzed in detail in ref. (*46*), served us as reference for validation purposes. Following the notation of ref. (*46*), we selected the brightest pixel of the cloud n°1, extracted from the VIMS cube 1481598962 (**Fig. S7A**). We first calculated the surface albedo over a cloud-free pixel close to the selected cloud pixel (**Fig. S7B**). Then the spectrum of the cloud pixel is inverted, fixing its surface albedo as the one retrieved from the spectrum of the cloud-free pixel. To invert the cloud properties, we ran the same genetic algorithm as for the inversion of the T56, T65 and T70 spectra, under the same conditions (initial population, gene length, crossover and mutation probabilities, parameters, and parameter ranges of variation – except for altitude that is extended to 60 km). The TB cloud spectrum and the results of our tests are shown in **Fig. S7C**. We were not able to fit the data with a cloud composed of tholins, especially in the 5-µm atmospheric window where such a cloud presents a systematic excess of reflectivity. Conversely, the liquid methane cloud gives an excellent fit to the observation, with best-match calculated top altitude (~40 km) and optical depth (~0.2) in excellent agreement with results of ref. (*46*). These tests lead to the conclusion that our model is able to make the difference between a cloud composed of solid organic particles and a cloud composed of liquid methane droplets in a robust way, bringing very good confidence in the inversion of T56, T65 and T70 event spectra.

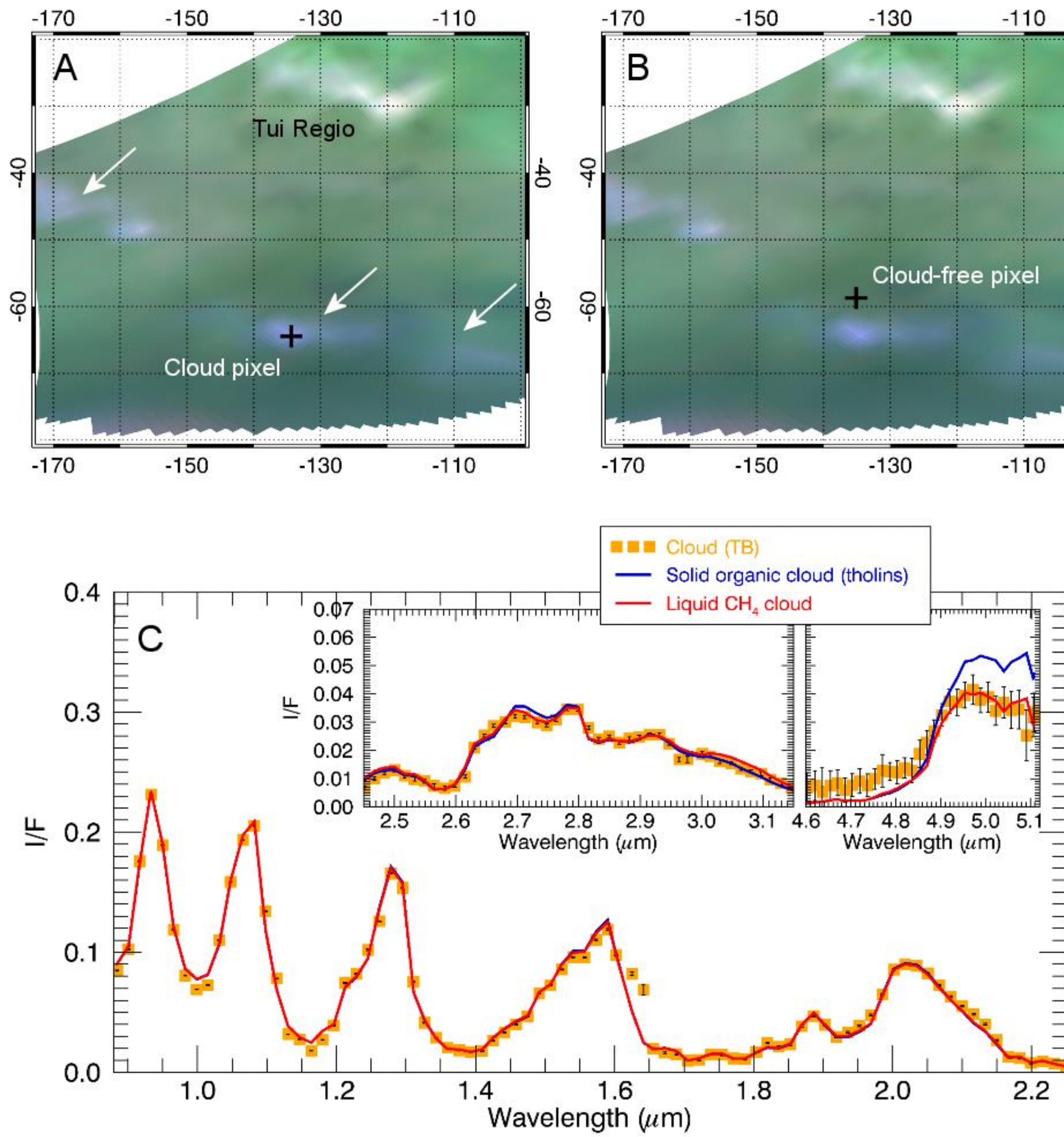

Fig. S7. Testing our model on a methane cloud observed by VIMS on 26 October 2004 (TB flyby). (A) Cylindrical reprojection of the VIMS cube 1481598962 using a RGB color composite of the 5-µm (red), 2.01-µm (green) and 2.78-µm (blue) bands. The white arrows point to the methane clouds visible in the image. Tui Regio, a bright surface area, can also been seen. We extracted and analyzed the spectrum of the brightest pixel (black cross) of the central cloud in the image (corresponding to the cloud n°1 analyzed in ref. (*46*)). **(B)** We also extracted the spectrum of a cloud-free pixel nearby the cloud (black cross) to be used as representative of the albedo of the surface below the cloud. **(C)** Comparison between the observed spectrum (orange squares, along with 1σ error bars due to data SNR) and the best-match spectra calculated by our radiative transfer model, considering a cloud composed of either solid organic particles (blue) or liquid methane droplets (red). The overall best fit with the data was obtained with a liquid methane cloud, with the following properties: a top altitude of ~40 km, an optical depth of ~0.2 at 2-μm and an effective droplet diameter of ~20-100 microns, in excellent agreement with the results of ref. (*46*).

3.5.3 Are the methane cloud retrieved by our model physically possible?

Cloud simulations using the TRAMS model[26,27] have been conducted using conditions (temperature and wind profile) obtained from the IPSL Titan GCM[38,47] at the season and location of the dust storm observations (**Fig. S8**). TRAMS is not specifically a convective cloud model, but a general purpose cloud model that can simulate both convective and stratiform clouds. While the IPSL Titan GCM input temperature and wind profiles are unlikely to be an exact representation of reality, they are probably reasonably close given that the overall global variation of tropospheric temperature is thought to be relatively invariant with season. The IPSL Titan GCM temperature profile is shown below, as plotted on a skewT-logP thermodynamic diagram (red curve).

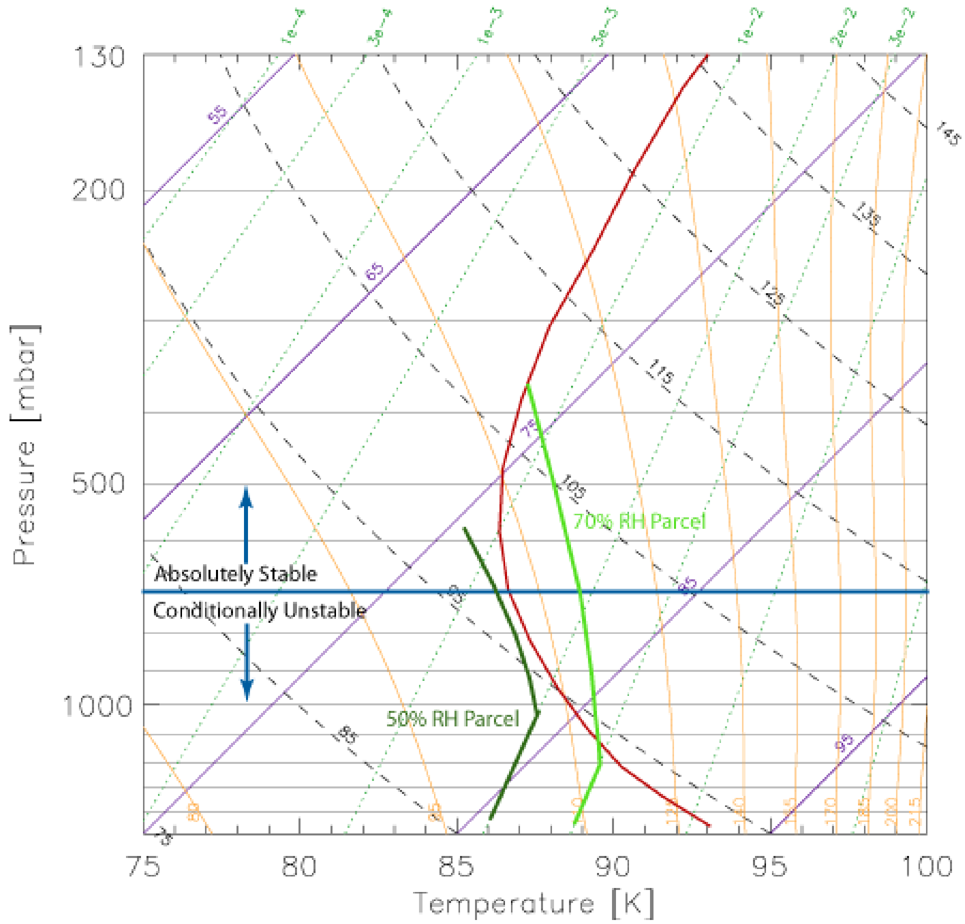

Figure S8. IPSL Titan GCM sounding plotted on a SkewT-LogP thermodynamic diagram. The red line is temperature. The light green line shows a hypothetical 70% surface relative humidity condition. The green line shows a hypothetical 50% relative humidity profile.

The moisture profile is likely far more important than temperature when it comes to clouds, but it is not well constrained by observations, and the values derived from models are highly dependent on a variety of poorly constrained assumptions. However, a range of scenarios can be considered.

Below the 700 mb level (below 13 km), the atmospheric lapse rate is greater than the moist adiabatic lapse rate; if the atmosphere is saturated at any location below 700 mb it will spontaneously result in deep, moist convection. If there were shallow near-surface clouds (i.e., a relative humidity (RH) of 100%), these clouds would be unstable and would rapidly produce extremely deep convection. There is virtually no convective inhibition—the level of free convection is the lifting condensation level. Thus, based on any temperature profile reasonably close to the IPSL Titan GCM profile shown in **Figure S8**, methane clouds with a top at and below 700 mb (13 km) can be ruled out strictly from thermodynamic principles.

Now consider sub-saturated conditions. A parcel with a surface relative humidity of 70% (mixing ratio of 3×10^{-2}) would have to be lifted to 1200 mb (3.5 km) to saturate and then another 50 mb to reach positive buoyancy, as shown by the light green parcel trajectory on the above figure. At that point, the parcel would ascend to nearly 350 mb (25 km). Importantly, the level of free convection and the lifting condensation level are nearly identical. At humidities greater than 70%, a small amount of lifting would produce very strong convective clouds with depths of many tens of kilometers. If any parcel with a humidity of 70% or greater is lifted, a convective methane cloud, not stratiform, will be produced and it will be deep, not shallow. These clouds are completely inconsistent with any interpretation of the observations.

With a surface mixing ratio of 50% RH (mixing ratio of 2×10^{-2} shown by the dark green curve), the negatively buoyant parcel would have to be lifted to 1050 mb (i.e., over 400 mb of depth, or 6 km) to saturate, which would be a grand energetic challenge, and no amount of lifting would ever result in a convective cloud. It may be concluded that no clouds are likely for humidity less than 50%, due to the difficulty in lifting the parcel over such a great distance, and even if it were accomplished, the cloud would be stratiform in nature and shallow due to negative buoyancy associated with further lifting.

If we wish to produce a surface-based convective cloud with a depth of ≈10 km, similar to the observational best fits, the humidity would have to be ≈55%. Such a parcel would still require substantial lifting to produce a cloud (the lifting condensation level), and even more lifting before it was positively buoyant (the level of free convection). While this cannot be ruled out, it seems very unlikely and would require an argument of special times where the humidity was just right (down to fractions of a percent) to produce a cloud of just the right depth: just a smidge too little and no cloud; just a smidge too much, and a deep convective cloud up to 25km or more. To illustrate this, results from the TRAMS model for a humidity of 60% is shown below (**Fig. S9**). Note that to even generate this cloud, a substantial initial thermal perturbation was necessary to lift the parcel the LCL and LFC. Microphysical results aside, the depth of the cloud is seen to extend to heights above 25 km, which is inconsistent with any interpretation of the observations.

Similar arguments rule out convective clouds resulting from non-surface air parcels. For example, a saturated parcel originating at 800 mb could produce a shallow convective cloud of approximately the right depth. But, any lower and the cloud would be too deep, and any higher and the cloud would be far too shallow (or there would be no cloud at all). In summary, the temperature profile is not conducive to producing a convective cloud of ≈10 km depth without invoking extraordinary lifting mechanisms combined with an extremely narrow range of permissible humidity.

Above the 700 mb level (>13 km), the atmosphere is absolutely stable; any saturated air parcel at or above this level will not experience a vertical acceleration and will result in a stratiform cloud. None of the retrievals are consistent with a cloud at this height. Further, one must argue for a ≈10 km thick region of saturation with microphysical properties that are consistent with the observational best fits. Perhaps more importantly, the saturated region must also be spatially confined. There is no known physical mechanism that could produce a deep saturated layer that is locally confined. Thus, the region where stratiform clouds could possibly form is completely inconsistent with any interpretation of the observations in terms of methane cloud.

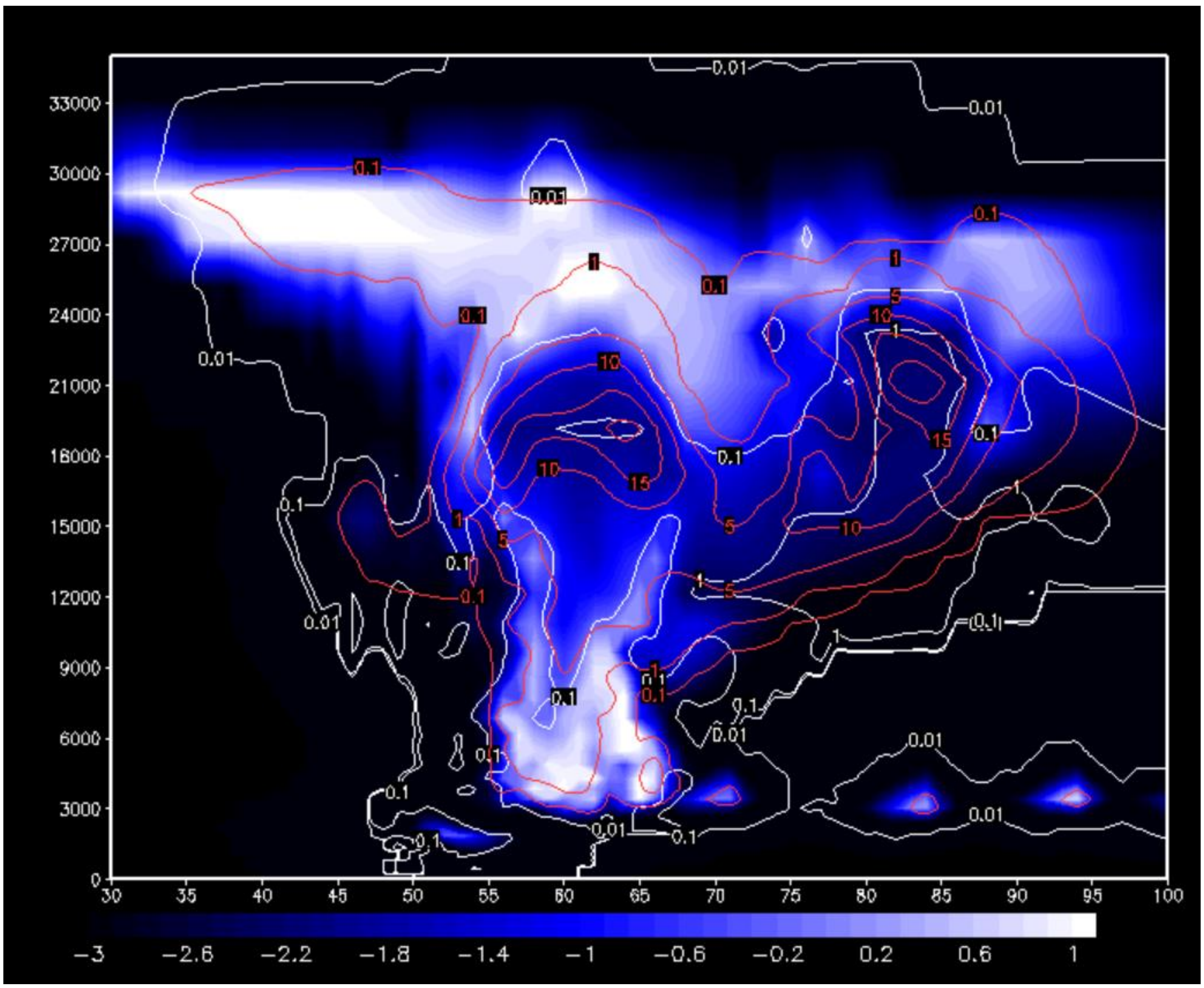

Figure S9. Results for a surface humidity of 60% from TRAMS (with an equatorial and equinoctial temperature and wind profiles coming from the IPSL Titan GCM). Shaded colors are $\log_{10}$ of number concentration (cm^{-3}). White contours are average particle radius (mm), and red contours are cloud condensate mixing ratio (g/kg). The cloud extends to well over 25 km in altitude.

Even though thermodynamics alone are sufficient to discount methane clouds, microphysical information from the TRAMS model are also completely inconsistent with the aerosol retrievals. Looking again at **Fig. S9**, the lower portion of the cloud updraft is found to have a relatively large number ($\approx 10\ cm^{-3}$) of small droplets (lower than 0.1 mm). As these rise further into the cloud, the number concentration drops (due to collision and coalescence) and the size increases (due to collision and coalescence and vapor growth). At about 20 km altitude, the number concentration is less than 0.1 cm^{-3}, and the size is greater than 1mm. Besides, the resulting total cloud opacity is largely greater than 10. None of these properties (top altitude, average particle size and number density, and cloud total opacity) are consistent with observations.

Stratiform clouds are likely to be more consistent with the anvil of the cloud. It is not physically possible to simulate clouds below 13 km, because those types of clouds are not physically possible given the thermodynamic sounding. Nevertheless, even the anvil clouds are completely inconsistent with the retrieved putative methane cloud properties.

In summary, the retrieved clouds are restricted to altitudes below ≈13 km and probably lower. Any clouds with a base below this level would be convective in nature and would extend to much greater altitudes. The microphysical properties are also completely inconsistent with the retrievals. Stratiform clouds below ≈13 km are not physically possible due the conditional instability of the sounding.

4. Sediment motion thresholds

We modify for Titan models of the fluid threshold (the minimum friction velocity above which sediment transport can be sustained) which were originally developed for the Earth, Mars and Venus[31-33]. The fluid threshold can be estimated using semi-empirical expressions[31,32] or calculated from numerical simulations or analytical formulae[33]. Since the physics of sediment transport is largely similar from one planet to another (i.e. the shear stress on a grain controls the sand transport), the values of the thresholds on Titan only have to be scaled to the moon's local properties (gravity, air viscosity, concentration and mass density, sediment mass density, interparticle forces – **Table S6**). **Figure 3** in the main text shows the fluid thresholds we estimated for a range of possible mass densities (800-1200 kg.m^{-3}) and interparticle forces (parameter γ = 1-5.10^{-4} N/m) for Titan's sand material[32], calculated with the different aforementioned transport models. The minimum friction velocity at fluid threshold to initiate saltation under Titan's lower atmosphere conditions is found to be ~0.04-0.09 m/s (corresponding to a wind of ~1.35 m/s at 40 m altitude, considering a surface roughness length of 0.005 m (ref. *(35)*) for particles with an optimum diameter ~300 µm. The threshold for sand-sized dust aggregates of similar size would be lower, and dependent on the exact density of the aggregate. The calculated threshold curves are in very good agreement with recent wind-tunnel measurements[40].

Table S6. Parameters (or ranges of parameters) used to calculate the fluid thresholds on Titan (see Fig. 3). [a] calculated from ref. (*48*). [b] from ref. (*49*). [c] from ref. (*32*).

Gravity ($m.s^{-2}$)	Air dynamic viscosity[a] ($kg.m^{-1}.s^{-1}$)	Air number density[b] (m^{-3})	Air mass density ($kg.m^{-3}$)	Sediment mass density ($kg.m^{-3}$)	Interparticule force parameter (γ)[c] ($N.m^{-1}$)
1.352	6.37×10^{-6}	1.15×10^{14}	5.24	800-1200	$1\text{-}5 \times 10^{-4}$

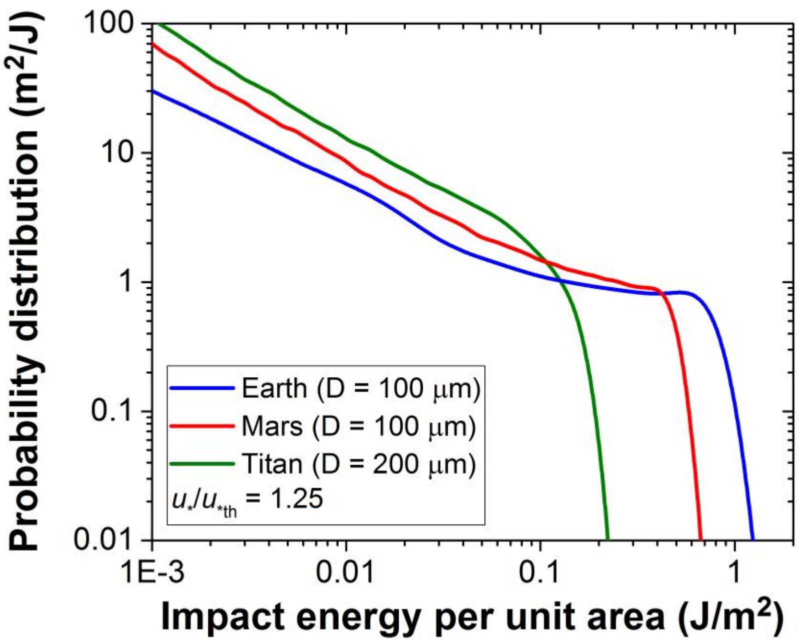

Fig. S10. Probability distributions of the energy per unit area with which saltating particles impact the sand bed, simulated by the numerical saltation model COMSALT[50] for Earth (blue line), Mars (red line), and Titan (green line) conditions. All simulations are for $u^* = 1.25u^*_{th}$, where u^*_{th} refers to the minimum shear velocity above which saltation can be sustained, which corresponds to ~0.16 m/s for 100 µm particles on Earth (e.g., ref. (*32*)), ~0.12 m/s for 100 µm particles on Mars[34,51], and ~0.05 m/s for 200 µm particles on Titan[40].

Supplementary references

41. E. Quirico, B. Schmitt, Near-infrared spectroscopy of simple hydrocarbons and carbon oxides diluted in solid N2 and as pure ices: Implications for Triton and Pluto. *Icarus* **127**, 354-378 (1997).

42. B. N. Khare *et al.*, Optical constants of organic tholins produced in a simulated titanian atmosphere: From soft X-ray to microwave frequencies. *Icarus* **60**, 127-137 (1984).

43. P. Rannou *et al.*, Titan haze distribution and optical properties retrieved from recent observations. *Icarus* **208**, 850-867 (2010).

44. R. Dimeo, K.Y. Lee, The use of a genetic algorithm in power plant control system design. Proceedings of the 34th Conference on Decision & Control, New Orleans, LA (December 1995).

45. D. Marquardt *et al.*, An Algorithm for Least-Squares Estimation of Nonlinear Parameters. *Journal of the Society for Industrial and Applied Mathematics* **11**, 431–441 (1963).

46. C. A. Griffith *et al.*, The Evolution of Titan's Mid-Latitude Clouds. *Science* **310**, 474-477 (2005).

47. S. Lebonnois, J. Burgalat, P. Rannou, B. Charnay, Titan global climate model: A new 3-dimensional version of the IPSL Titan GCM. *Icarus* **XXX**, XXX-XXX (2012).

48. M. Z. Jacobson, Fundamentals of Atmospheric Modeling (Cambridge Univiversity Press, 1999).

49. E. Lellouch *et al.*, Titan's atmosphere and hypothesized ocean: A reanalysis of the Voyager 1 radio-occultation and IRIS 7.7-µm data. *Icarus* **79**, 328-349 (1989).

50. J. F. Kok, N. O. Renno, A comprehensive numerical model of steady state saltation (COMSALT). *J. Geophys. Res.* **114**, D17204 (2009).

51. J. F. Kok, An improved parameterization of wind-blown sand flux on Mars that includes the effect of hysteresis. *Geophys. Res. Lett.* **37**, L12202 (2010).